Development of a fast, accurate radiative transfer model for the Martian atmosphere, past and present

Michael A. Mischna,[1] Christopher Lee,[2] and Mark Richardson[2]

Received 23 April 2012; revised 2 August 2012; accepted 9 September 2012; published 19 October 2012.

[1] We present details of an approach to creating a *k*-distribution radiative transfer model (KDM) for use in the Martian atmosphere. Such models preserve the accuracy of more rigorous line-by-line models, but are orders of magnitude faster, and can be effectively implemented in 3-D general circulation models. The approach taken here is sufficiently generalized that it can be employed for atmospheres of any arbitrary composition and mass, and demonstrations are provided for simulated atmospheres with a present-day Martian surface pressure (~6 mb) and a putative thick early Mars atmosphere (~500 mb), both with and without atmospheric water vapor. KDM-derived absorption coefficients are placed into a look-up table at a set of gridded points in pressure, temperature and atmospheric composition, and a tri-linear interpolation scheme is used to obtain the coefficients appropriate for the local atmospheric conditions. These coefficients may then be used within any of a variety of commonly used flux solvers to obtain atmospheric heating rates. A series of validation tests are performed with the KDM for both present-day and early Mars atmospheric conditions, and the model is compared against several other widely used radiative transfer schemes, including several used in contemporary general circulation models. These validation results identify weaknesses in some other approaches and demonstrate the efficacy of the KDM, providing a rigorous test of these types of models for use in the Martian atmosphere. A demonstration of results obtained by implementing the KDM in a Mars general circulation model is provided.

Citation: Mischna, M. A., C. Lee, and M. Richardson (2012), Development of a fast, accurate radiative transfer model for the Martian atmosphere, past and present, *J. Geophys. Res.*, *117*, E10009, doi:10.1029/2012JE004110.

1. Introduction

[2] There is a growing need for fast, flexible and accurate approaches to modeling the Martian atmosphere. Our understanding of the dynamics and physics of the Martian atmosphere has matured to such a degree that we must be able to capture the influence of a variety of atmospheric constituents (both gases and aerosols) if we wish to accurately calculate atmospheric heating rates and, subsequently, atmospheric motion. While the dominant radiatively active component of the present Martian atmosphere is carbon dioxide (95.3% by volume), and other radiatively active gases are found only in trivial amounts (water vapor being key among these), during past epochs, the environment was substantially different, likely with a thicker CO_2 atmosphere and a greater abundance of other gases, potentially including H_2O, sulfur dioxide, methane and others, each of which may have been radiatively significant for either short durations, or for longer periods.[1]

[3] During the past several decades, a number of approaches were developed to tackle the problem of radiative transfer on present-day Mars [*Pollack et al.*, 1981; *Crisp et al.*, 1986; *Pollack et al.*, 1990; *Hourdin*, 1992]. Typically, these approaches took the form of wide-band models, and took an empirical approach to reproducing the amount of atmospheric absorption present in the infrared and visible spectrum within spectral bands of greatest absorption. These approaches are generally very fast, and easily conducive to implementation in general circulation models (GCMs).

[4] As the level of sophistication in GCMs rises, they become increasingly capable of simulating a broader range of atmospheric conditions and processes on Mars. These include such present-day phenomena as global dust storms and water ice cloud belts, but also conditions present in recent Martian history (10^4–10^6 Ma) such as changes in obliquity and other orbital parameters, and in ancient Martian history (10^8–10^9 Ma) when the atmospheric composition and mass may have been substantially different than the present-day. Geological and geochemical studies of the Martian surface [*Carr*, 1996; *Solomon et al.*, 2005] have convincingly

[1]Jet Propulsion Laboratory, California Institute of Technology, Pasadena, California, USA.
[2]Ashima Research, Pasadena, California, USA.

Corresponding author: M. A. Mischna, Jet Propulsion Laboratory, California Institute of Technology, 4800 Oak Grove Dr., M/S 183-601, Pasadena, CA 91109, USA. (michael.a.mischna@jpl.nasa.gov)

0148-0227/12/2012JE004110

[1]Auxiliary material data sets are available at ftp://ftp.agu.org/apend/je/2012je004110. Other auxiliary material files are in the HTML. doi:10.1029/2012JE004110.

pointed to an early Mars that had a rather different environment than today's cool and dry conditions. With widespread evidence of global surface water for extended periods through the Noachian and Hesperian periods found in the rock record, and potentially punctuated episodes of liquid water through to the present-day, it is tempting to draw the conclusion that the climate must have been significantly more clement than today, with a thicker, warmer atmosphere and potentially non-trivial amounts of water vapor and other atmospheric trace gases. As such, there has been increased interest in linking Martian climate studies to the fields of geology and geochemistry. In order to simulate these vastly different conditions, new and more sophisticated approaches to Mars climate modeling must be pursued—approaches that can accommodate differing atmospheric pressures and compositions, among other conditions. Unfortunately, the aforementioned wide-band radiative transfer approaches are insufficiently flexible to deal with the purported ranges of pressure and composition, and they become increasingly restricted to a small set of climate problems. It becomes desirable, then, to find more sophisticated approaches to radiative transfer that are not computationally prohibitive in a GCM context, yet sufficiently accurate and flexible to be applied to a wide range of atmospheric conditions.

[5] One widely embraced approach, at least within the terrestrial community, to addressing these more sophisticated radiative transfer problems has been the adoption of the correlated-*k* method of modeling spectral absorption and emission by gases. In conjunction with a scattering model for aerosols, the correlated-*k* approach comprises a full treatment of gaseous and aerosol radiative transfer when integrated into a flux solver such as any of the commonly used two-stream frameworks. Correlated-*k* schemes retain much of the accuracy of precise line-by-line radiative transfer models, but are substantially faster, making them ideal for computationally expensive 3-D global models. The correlated-*k* approach dates back to the 1930s for studies of both stellar and terrestrial atmospheres [*Ambartzumian*, 1936; *Lebedinsky*, 1939], but it was only in the 1990s when a revival in the terrestrial literature [e.g., *Lacis and Oinas*, 1991; *Fu and Liou*, 1992; *Chou*, 1992; *Chou and Lee*, 1996; *Mlawer et al.*, 1997; *Kato et al.*, 1999] highlighted the true power and flexibility of the approach.

[6] The planetary community has been slower in adopting this method. The efficacy of the correlated-*k* approach on various terrestrial bodies over a range of conditions has recently been demonstrated using 1-D radiative convective models of early Earth [*Haqq-Misra et al.*, 2008; *von Paris et al.*, 2008], Venus [*Eymet et al.*, 2009] and generic CO_2-rich atmospheres [*Halevy et al.*, 2009; *Wordsworth et al.*, 2010]; however, incorporation into full GCMs, with few notable exceptions [e.g., *Johnson et al.*, 2008], has not become standard practice. Of the atmospheres of terrestrial planets, that of Mars has been the most robustly explored and has seen the broadest development in climate modeling. The correlated-*k* method remains on the periphery of Mars GCM modeling, however, because of its relative computational expense and seeming complexity, despite the fact that the Mars GCM community has been aware of these approaches for some time as evidenced by several abstracts, conference proceedings and webpages referencing correlated-*k* for Mars. Our aim is to give a demonstration of the robustness of the approach within the Martian atmospheric setting and provide a cross-validation of our implementation of the method with many other approaches. We hope, by doing so, to in part broaden the exposure of the GCM modeling community to this approach, allowing it to become a more widely adopted technique.

[7] In this paper, we will build on the terrestrial foundation to provide a formal description of the various components necessary to generate a working correlated-*k* model for gases in planetary atmospheres. Aerosols are not discussed, as scattering solvers are well described [e.g., *Briegleb*, 1992]. Presently, we will set forth how, in *practical* terms, such a model can be designed for use with the Martian atmosphere, and establish a framework for the reader to follow. In the subsequent sections will be a discussion of how one who is interested in such problems may go about developing, refining or validating their own correlated-*k*, or *k*-distribution model. (Within, we use the terms 'correlated-*k*' and '*k*-distribution' somewhat interchangeably, but make clear the distinction below). Where appropriate, references to the underlying theory and previous work will be provided. At the highest level, we bifurcate the discussion of these models into two distinct sections. First, we discuss how one may efficiently reproduce the absorption spectrum of the Martian atmosphere, including continuum and collision-induced effects and absorption by multiple gases, which may be important for early Martian atmospheres. The spectrum is constructed using a line-by-line model developed for this purpose. Second, we discuss how this very complex absorption spectrum can be reduced in such a way that it can be ingested by a GCM in a functional and efficient way. The exact scheme described here has been implemented in a variety of 1-D and 3-D climate models, including the MarsWRF GCM [*Lee et al.*, 2011] and the Ashima/MIT Mars GCM [*Lian et al.*, 2012]. We henceforth refer to it as the *k*-distribution model (KDM).

2. Correlated-k Theory

[8] The underlying driver of atmospheric motion is the net heating of the atmosphere through absorption and emission of visible and infrared radiation. Energy absorbed by atmospheric molecules is converted into translational motion proportional to its thermal temperature. The correlated-*k* method, (as with other approaches) seeks to quantify the amount of electromagnetic radiation absorbed by the myriad atmospheric constituents. Absorption has maxima at discrete wavelengths, depending on the molecule. A typical absorption spectrum may look something like the portion shown in Figure 1a. The highest resolution line-by-line (LBL) models calculate absorption with a spectral resolution much finer than the width of the individual lines, producing very accurate representations of atmospheric absorption, but at an extremely high computational cost (refer to, e.g., *Liou* [2002]). Because the radiative transfer calculations need to be repeated as the local conditions (temperature, pressure and composition) change, the radiative heating must be recalculated frequently and, as such, this makes use of the LBL models impractical. These line-by-line models have a limited use in climate studies, and primarily serve as a benchmark or validation for other approaches.

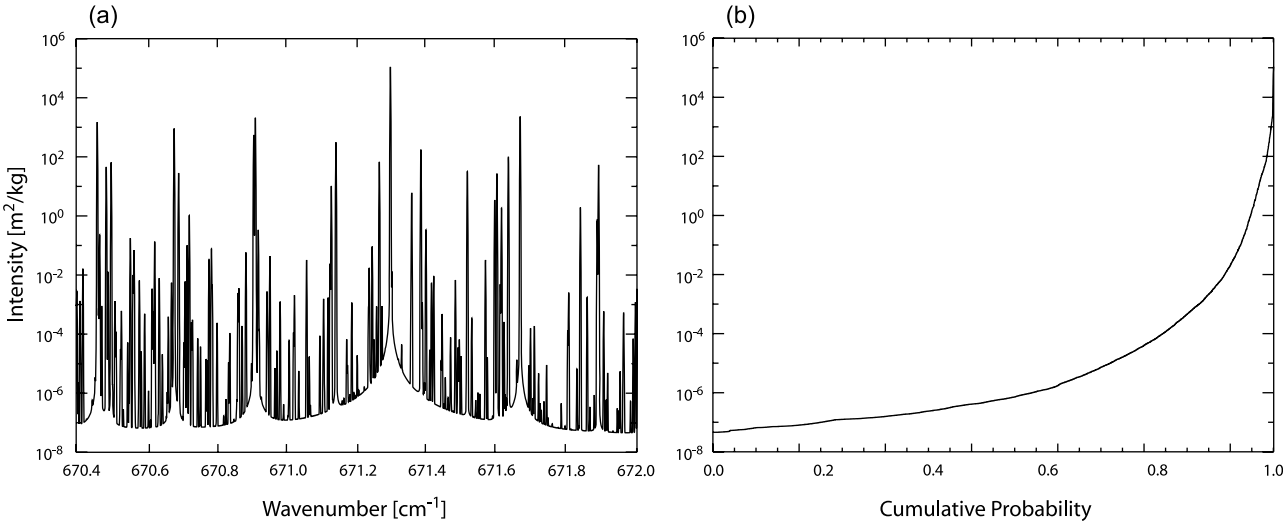

Figure 1. Comparison of a portion of the 15 μm spectrum both (a) unsorted and (b) sorted by strength as a *k*-distribution. The sorted spectrum is substantially smoother than the unsorted spectrum, and the curve can be well approximated by few points.

[9] The key numerical method used by the correlated-*k* algorithm to reduce the computational burden of the radiative transfer calculations involves re-sorting these individual, monochromatic absorption intensities into a smooth function that is more conducive to numerical approximation or fitting (Figure 1). Here, the smooth curve illustrated in Figure 1b contains the same intensity information as Figure 1a, but the curve in this region has now been sorted by magnitude, yielding a cumulative probability function of intensity, i.e., a function indicating the fraction of intensities smaller than the given value. The most costly calculations in radiative transfer are not in these manipulations of absorption coefficients, but in the calculations that convert these atmospheric absorption coefficients into heating rates. Thus, if we can minimize the number of the latter calculations in some fashion, we can greatly speed up our radiative transfer solution.

[10] For a standard line-by-line calculation, atmospheric transmissivity, *Tr* for a spectral band between wavelengths $\nu_{\min}$ and $\nu_{\max}$, is calculated as

$$Tr = \int_{\nu_{\min}}^{\nu_{\max}} \exp[-k_\nu u]\, d\nu, \tag{1}$$

where k_ν is the absorption coefficient (intensity) at frequency ν, and u is the mass of the absorbing gas along the path in question, (the product ku is more commonly referred to as opacity, τ). Following the re-sorting of the spectral band as discussed above, transmissivity can be equivalently defined as

$$Tr = \int_0^1 \exp\left[-k_g u\right] dg, \tag{2}$$

where now k_g is the absorption coefficient for the cumulative probability, g (ranging from zero to unity; see *Lacis and Oinas* [1991] for the mathematics of this conversion). Along with wavelength, the absorption coefficient is also a function of pressure, temperature and composition (see section 3), and will therefore vary depending on the local conditions in the atmosphere. In this form, k_g provides no computational advantage over k_ν—the absorption coefficients have merely been re-ordered. In the next section, we will discuss ways to approximate the k_g function, which is where the true advantage of the correlated-*k* approach lies.

[11] For a homogeneous path, equation (2) provides an exact solution for transmissivity, and the correlated-*k* approach is sometimes alternately referred to simply as a '*k*-distribution'. The 'correlated' aspect of correlated-*k* applies when this method is used for atmospheres along inhomogeneous paths. Due to pressure- and temperature-dependent effects, the overall shape of the spectrum will vary, even for a fixed atmospheric composition. Such inhomogeneous paths are handled by partitioning the continuously varying atmosphere into discrete 'layers' (an approach familiar to anyone involved in numerical modeling of atmospheres), each with a representative pressure and temperature, and with the sorting process being performed separately for each layer. Since the *k*-distribution method 'shuffles' the wavelength information independently for each layer, it is not assured that, say, the strongest absorption value for any one layer will be the same for even an adjacent layer (since absorption is a function of both vertically varying T and p). Typically, the shuffled order will be nearly the same between adjacent layers, but will become increasingly different between distant layers [*Fu and Liou*, 1992]. Because the same value in the cumulative probability distribution does not likely uniquely map back to the same wavelength for all atmospheric layers, this can result in the over- or under-absorption of photons when this method is employed. The only time photons are exactly accounted for is if the spectra are perfectly correlated—in other words, if there *is* a direct one-to-one mapping between wavelength and cumulative probability, and the mapping is unique throughout the atmosphere. For inhomogeneous paths, this is never the case, and any application of this method must accept some level of non-correlation. Fortunately, with a prudent selection of

spectral bands, the errors introduced by this non-correlation are generally limited, though results must be compared to a proper line-by-line calculation if assessment of the actual level of error introduced is desired. The assumption, however, that the levels are generally correlated to a high degree is typically valid, and is from whence the method derives its name.

[12] In the subsequent sections, we outline the approach for a user to implement a KDM through the following series of steps, which begins with the pre-computation of a table of absorption coefficients. *Johnson et al.* [2008], which used a similar *k*-distribution scheme, provided a high-level description of several of these steps, but with insufficient detail to fully implement the KDM. In greater detail, the steps are to: (1) Choose appropriate pressure, temperature, wavelength and atmospheric gas mixtures under which absorption coefficients are desired. (2) Create a high resolution, line-by-line representation of the spectrum for each atmospheric state in step 1, from data in HITRAN and assuming a standard (e.g. Voigt) lineshape. (3) Modify the lineshape as required and incorporate continuum and other absorption features (e.g., collision-induced or dimer absorption) into the spectrum. (4) Merge spectra from individual gases to form single atmospheric spectrum. (5) Sort the convolved spectrum by line strength. (6) Perform Gaussian quadrature integration of sorted spectrum to obtain *k*-values and weights to be used in a climate model radiation code (for example, within a two stream flux solver).

[13] Each of these steps will be discussed in turn in the sections below, providing the reader with sufficient procedural information to successfully implement this approach.

3. Implementation

3.1. Establishing Atmospheric Conditions of Absorption

[14] Being a function of local temperature and pressure, the absorption coefficient, k_ν, for a gas at wavelength ν will vary significantly throughout the atmosphere and, for a generic planetary atmospheres being modeled in a GCM, it typically becomes necessary to pre-compute absorption coefficients over a wide range of temperature and pressure conditions encompassing those expected to be observed. As noted above, our description of this approach applies specifically to the Martian atmosphere although the same approach may be followed for other planetary atmospheres with the proper substitution of relevant physical parameters (e.g., gravity, specific heat) and adjustments to the spectrum relevant to the ambient gas mixture.

[15] While present-day surface temperatures on Mars fall within the range ~150–280 K, in the upper atmosphere, temperatures dip to 100 K or below. At the other extreme, temperatures experienced in the Martian past may have been as high as 300 K or greater [*Johnson et al.*, 2008] and potentially many hundreds of Kelvin higher than this in the aftermath of large impacts [*Segura et al.*, 2008]. Mean surface pressure presently averages ~6 mb, but may have been as great as several bars early in Martian history, while in the upper atmosphere, pressures are many orders of magnitude smaller than this. To ensure we can quantify absorption across this full range of potential pressure/temperature (p/T) conditions, we take a gridded approach and create a look up table (LUT) that spans a temperature range 50–400 K and pressure range 10^{-4}–10^{6} Pa (1 nb to 10 bar) that fully encapsulates the range of conditions that may plausibly be or have been observed on Mars throughout its history (see auxiliary material for the LUT used in this study along with codes to read in the LUT). Within our grid, we have selected spacing of 20 K in temperature and 0.4 in $\log(p)$. The choice of grid spacing is a balance between accuracy and ease of development, and our choice of steps is the result of numerous tests with various step sizes. To obtain the coefficients appropriate for any local (p, T) combination, bilinear interpolation is applied in T and $\log(p)$ across the nearest table elements. Reducing the grid spacing further in either pressure and temperature results in a linear increase in table generation time, but only a negligible change in the resultant absorption coefficients (and, subsequently, heating rates), whereas an increase from the chosen values result in an increasing deterioration of accuracy in the final atmospheric heating rates (see section 5).

[16] Given a 2-D pressure and temperature grid over which to calculate absorption coefficients, the next step in the KDM development process is the partitioning of the full visible/IR wavelength spectrum into a number of discrete 'bands,' (for planetary temperatures, wavelengths outside the visible/IR region can be neglected—UV absorption may be treated external to this approach [e.g., *González-Galindo et al.*, 2005]). It is not possible to apply this method to the entire spectrum as a whole. As mentioned in the previous section, radiative transfer, at its highest level, can be seen as the accounting of photons in the atmosphere; the success of the KDM is highly tied to this perception. To further extend this view, by limiting the width of an individual spectral band, it is ensured that the number of photons initially incident at each monochromatic wavelength within the band is approximately constant, and that each wavelength is therefore equally weighted with respect to all others in the band. (In simpler terms, we can only perform the re-sorting of lines from k_ν to k_g because we make the implicit assumption that all re-sorted wavelengths experience an equal number of source photons, either solar or IR, and that no one wavelength is more 'important' than any others—equivalent to assuming a constant Planck function within the band.) Hence, we cannot simply re-sort the entire spectrum as a whole, as the number of incident photons across the spectrum varies substantially. For our Mars implementation (or for any atmosphere in which CO_2 is a dominant gas) we choose to partition the spectrum into 14 bins spanning the visible and IR spectrum (from 10 to 41,666 cm^{-1}, or 0.24 to 1000 μm), with seven bands in the visible, and seven in the infrared, according to Table 1.

[17] The choice of bands reflects a compromise between speed and accuracy in our LUT generation, and the limits were adopted from those employed by the Ames Mars GCM (R. Haberle, personal communication, 2005), but with the addition of two additional bands within the 15 μm region of the infrared. For more complex atmospheres containing additional trace gases, alternate wavelength binning may be performed, but care must be taken to follow the restrictions outlined above. Each of the 14 bands is essentially an independent entity, and absorption coefficients are calculated separately for each band, and stored independently in the LUT (adding to it a third dimension). Following this

Table 1. Band Limits Used in the MarsWRF Radiation Scheme

	Wave Number (cm^{-1})	Wavelength (μm)
Infrared	10–166	1000–60.24
	166–416	60.24–24.04
	416–625	24.04–16.00
	625–710	16.00–14.08
	710–833	14.08–12.00
	833–1250	12.00–8.00
	1250–2222	8.00–4.50
Solar	2222–3087	4.50–3.24
	3087–4030	3.24–2.48
	4030–5370	2.48–1.86
	5370–7651	1.86–1.31
	7651–12,500	1.31–0.80
	12,500–25,000	0.80–0.40
	25,000–41,666	0.40–0.24

approach, it becomes possible to measure the contributions of individual absorption bands to the atmospheric heating rate, if desired (such as the important 15 μm CO_2 band), or, by summing the respective bands, to calculate the net atmospheric heating rate.

[18] A final consideration, mentioned above, is the accommodation of multiple absorbing gases in the model atmosphere. For example, on early Mars, water vapor would have played a more significant role in the climate and, hence, its potential radiative effects should be captured in our LUT. In practical terms, this requires adding a fourth dimension to the LUT, one that spans the plausible CO_2/H_2O gas mixtures in the atmosphere. For Mars, we include calculations for a range of water vapor volume mixing ratios from 10^{-7} to 10^{-1} by decade, in addition to a water-free calculation. Mixing ratios less than 10^{-7} are found to have a negligible influence on heating rates. The water vapor mixing ratio in the Martian atmosphere may be spatially and temporally variable, whereas the CO_2 mixing ratio is assumed to be fixed at 0.953 (though if the water vapor mixing ratio is 10^{-1}, we set the CO_2 mixing ratio to 0.9). Thus, by linear interpolation in the logarithm of this dimension the correct absorption coefficients may be obtained for any given atmospheric composition at each model grid point.

[19] It is further possible to add additional gases with variable mixing ratios. Each subsequent gas adds, however, an additional dimension to the LUT, increasing its complexity. In circumstances where more than two gases are desired in an atmosphere, we attempt to make prudent estimates of the mixing ratio of the additional gases such that we can assign to them a fixed or constant mixing ratio. Doing so degenerates the additional dimension(s) while still allowing us to perform various targeted investigations (see *Johnson et al.* [2008] for a description of this approach).

[20] At this stage, we have established a 4-D LUT of a range of putative conditions in the Martian atmosphere, spanning pressure, temperature, wavelength and composition. Our nominal table consists of 26 pressures, 18 temperatures, 14 spectral bands and 8 compositions, for a total of ~52,000 distinct atmospheric conditions at which we calculate atmospheric absorptivities. This is a larger, more comprehensive, table than the one used in the Ames Mars GCM due to narrower spacing between points in pressure and temperature, but developing the LUT with such a size is eminently tractable given present-day computing power.

3.2. Generating the Spectrum

[21] With the LUT framework established, one must initiate the most computationally intensive portion of the process and generate a unique spectrum for each point in this four dimensional grid and subsequently derive the associated cumulative probability function. The interest here is in obtaining those parameters that will fully describe the shape of individual absorption lines (refer to Figure 1a) within a band such that all known spectral lines can be reproduced at high resolution. This is tantamount to operating a line-by-line spectral code, the process of which is described in the following two sections.

[22] Individual absorption coefficients (k_ν) are defined as the product of the line intensity, $S_{nn'}$, a simple line shape function, f, and various line shape modification terms. Many of these parameters can be found in the HITRAN2008 (High-Resolution TRANsmission) molecular absorption database [*Rothman et al.*, 2009], which serves as the starting point for generating our high-resolution spectra. A demonstration of the process using a single point in the 4-D grid serves as an example. All other points within the LUT are calculated the same way.

[23] As an initial step in our approach, the HITRAN2008 database is searched for all spectral lines of gases (and potentially their isotopologues) of interest within one of the 14 spectral bands. The integrated line intensity, $S_{nn'}$, at a reference temperature, T_{ref}, of 296 K, is a parameter directly obtained for each line from the HITRAN database and modified to reflect the local atmospheric conditions as shown in, e.g., *Rothman et al.* [1998],

$$S_{\eta\eta'}(T) = S_{\eta\eta'}(T_{ref})\frac{Q(T_{ref})}{Q(T)}\frac{\exp(-c_2E_\eta/T)}{\exp(-c_2E_\eta T_{ref})} \cdot \frac{[1-\exp(-c_2\nu_{\eta\eta'}/T)]}{[1-\exp(-c_2\nu_{\eta\eta'}/T_{ref})]}, \quad (3)$$

using other terms derived from the HITRAN database or associated packages. The first term on the right hand side is the reference spectral line intensity (at p_{ref} = 1 bar and T_{ref} = 296 K) from the HITRAN database. The remaining three terms modify this reference line intensity due to temperature-dependent changes in the total internal partition functions, Boltzmann populations and stimulated emission, respectively. Temperature-dependent total internal partition sums, $Q(T)$, are taken from *Fischer et al.* [2003], and the remaining values are obtained directly from HITRAN. The value E_η is the lower state energy of the transition, and $\nu_{\eta\eta'}$ is the spectral line transition frequency. The second radiation constant, c_2 is defined as hc/k and equals 1.4388 cm-K. The result is the strength of the line for the local temperature conditions.

[24] It is the line shape function, f, however, that dictates how the line absorption is distributed over wavelength. There is a wealth of literature devoted to theory and derivation of various lineshapes [e.g., *Goody and Yung*, 1995; *Liou*, 2002], and the reader is referred to these references for a more detailed explanation. For the Martian atmosphere, we choose

the widely used Voigt line shape, which convolves the effects of the Lorentz (pressure-broadened) line shape, predominating in the lower atmosphere, and the Doppler (Gaussian) line shape which is more significant in the thinner upper atmosphere. The Voigt lineshape function, at wavelength ν and for a line with central wavelength ν_0 is defined as:

$$f(\nu-\nu_0)=\frac{1}{\alpha_D}\sqrt{\frac{\ln 2}{\pi}}K(x,y), \tag{4}$$

where the Voigt function $K(x, y)$ is defined as

$$K(x,y)=\frac{y}{\pi}\int_{-\infty}^{\infty}\frac{e^{-t^2}}{y^2+(x-t)^2}dt \tag{5}$$

and

$$y=\frac{\alpha_L}{\alpha_D}\sqrt{\ln 2}\qquad x=\frac{\nu-\nu_0}{\alpha_D}\sqrt{\ln 2}\qquad t=\frac{\nu-\nu'}{\alpha_D}. \tag{6}$$

Here, α_L and α_D represent the Lorentz and Doppler halfwidths, respectively.

[25] The Voigt lineshape may be numerically approximated using one of many fast, numerical solutions [e.g., *Humlíček*, 1979, 1982; *Wells*, 1999]. We have applied an efficient subroutine developed by *Wells* [1999] to generate the Voigt shape of each line obtained from HITRAN in the previous step. Generation of the Voigt profile here requires knowledge of both the Doppler- and pressure-broadened halfwidths. The Lorentz halfwidth at standard (p/T) conditions is a parameter obtained directly from HITRAN, while the Doppler halfwidth is a function of the temperature and molecular mass of the gas.

$$\alpha_D=\nu_0\sqrt{\frac{2k_BT}{mc^2}} \tag{7}$$

where T is local temperature, m is the molecular mass of the gas, k_B is Boltzmann's constant and c is the speed of light. Temperature and pressure correction of the Lorentz line halfwidth (α_L, calculated at 296 K) in HITRAN is necessary:

$$\alpha_L(p,T)=\left(\frac{T_{ref}}{T}\right)^n\left(\alpha_{air}(p_{ref},T_{ref})(p-p_s)+\alpha_{self}(p_{ref},T_{ref})p_s\right). \tag{8}$$

The values of α_{air}, α_{self}, and n are obtained from HITRAN, and reflect the air-broadened halfwidth, self-broadened halfwidth and coefficient of temperature dependence, respectively. The partial pressure of the gas under consideration, p_s, discriminates between whether air-broadening or self-broadening is dominant, (thus the "dominant" gas in the Martian atmosphere, CO_2, is mostly self-broadened, while trace gases, such as water vapor, are almost exclusively air-broadened.) Reference conditions in equation (8) are p_{ref} = 1000 mb, and T_{ref} = 296 K, reflecting the terrestrial heritage of HITRAN. The use of air-broadened coefficients rather than CO_2-broadened coefficients (which are not available in HITRAN, but appropriate for Mars) will lead to slight errors in the line shape and overall spectrum.

[26] The formal definition of the Voigt lineshape (equation (4)) integrates the line intensity for wavelengths from 0 to ∞, which proves to be impractical in implementation. Various studies [*Segura et al.*, 2007, *Meadows and Crisp*, 1996; *Halevy et al.*, 2009] have investigated the distance from a line center for which these spectral 'wing' contributions are non-negligible and should be included in absorption calculations. While, alone, absorption from a single line far from its center is very weak, the accumulation of thousands or tens of thousands of such overlapping line wings can produce a non-negligible absorption referred to as the 'continuum'.

[27] Work by *Halevy et al.* [2009] has shown that discretization of a single line feature extending to at least several hundred wave numbers from the line center produces results that best match observations in contemporary atmospheres. Such a span, unfortunately, becomes impractical to numerically implement in many cases, especially at lower pressures where line widths are extremely narrow. Computationally, the calculation of these broad line wings may become prohibitive. In order to discretize the entire band so as to capture absorption from all spectral lines, we have chosen a spectral step, $\Delta\nu$ of 20% of the narrowest calculated Voigt halfwidth (irrespective of species) within each band. Thus, narrow line widths make it challenging to integrate across wide regions of the spectrum. (As an example, consider: for a spectral band with 10^5 spectral lines and a minimum line width of 10^{-8} cm^{-1}, calculating out 500 cm^{-1} along each wing (1000 cm^{-1} full width) from the line center for each line requires upwards of $10^5 \times 10^8 \times 10^3 = 10^{16}$ individual calculations to fully model the band). This is presently a computational challenge. In order to investigate the present-day Martian atmosphere, then, particularly at higher altitudes and low pressures—conditions where line widths are narrower, we must sacrifice absolute precision for practicality. We have found that for most of the infrared region at low pressure (bands 3–9 in Figure 2), it is only tractable to perform calculations for CO_2 out to 25 cm^{-1} from the line center, while in regions of the far IR (bands 1–2), in visible wavelengths (bands 10–14), and at higher pressures across all wavelengths, where line widths are generally broader, wing contributions can be calculated out to as much as 500 cm^{-1}. Water vapor is treated differently, as discussed below. Ideally, all lines would be calculated out to the same maximum extent, but through trial and error, we have established a map of pressure versus spectral band (Figure 2), using our nominal table pressure spacing, and showing the corresponding wing width that can be calculated for CO_2 within a reasonable time.

[28] To determine our spectral step $\Delta\nu$, we take 20% of the narrowest Voigt line halfwidth calculated in the spectral band. The Voigt halfwidth is approximated following the equation of *Olivero and Longbothum* [1977]

$$\alpha_\nu \approx 0.5346\alpha_L+\sqrt{0.2166\alpha_L^2+\alpha_D^2}. \tag{9}$$

for each line in the band. The shape of every individual line core will therefore be represented by no less than 10 points (and exactly 10 points across the full-width half-maximum

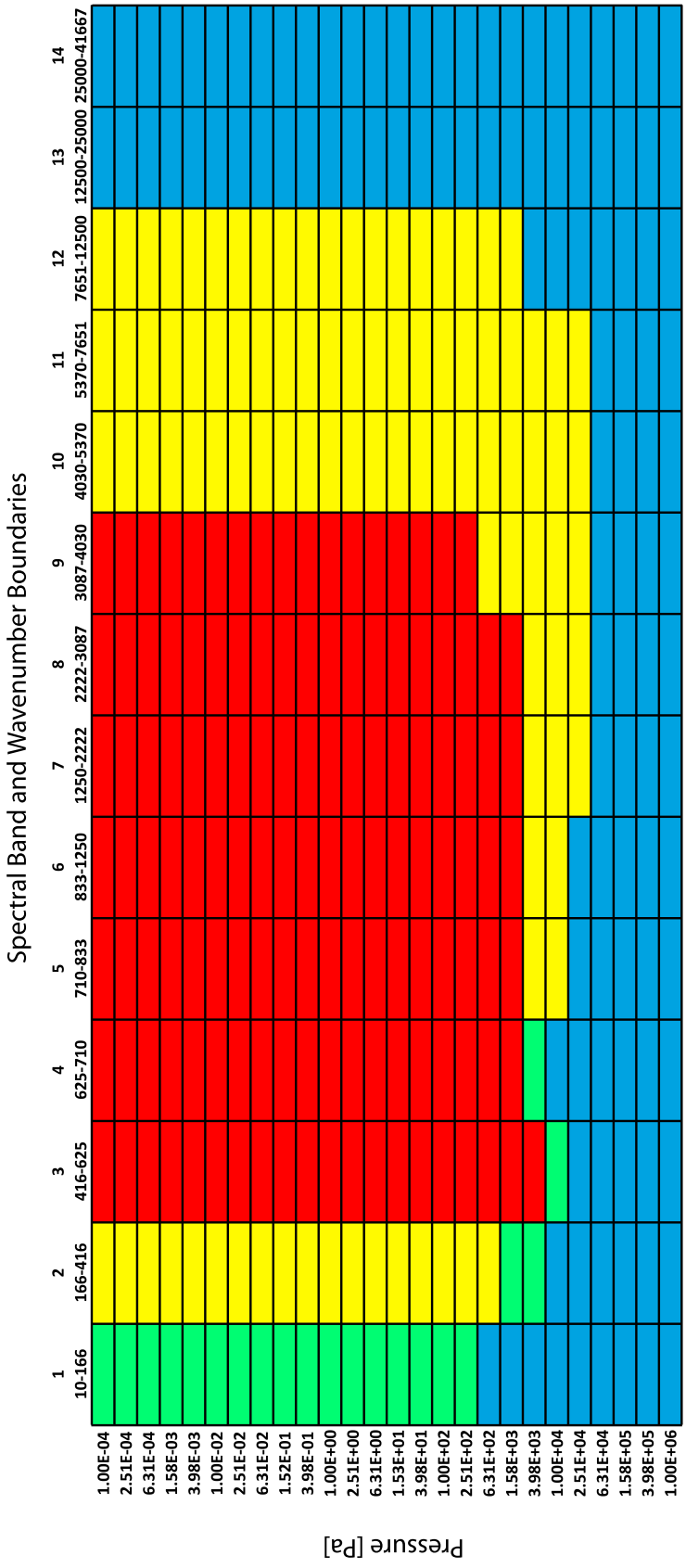

Figure 2. Wing width used in generation of KDM k-coefficients. Pressures range from 10^{-4} to 10^{6} Pa with a step of 0.4 in log(p). Boundaries (in cm^{-1}) of the 14 bands used in the KDM are found along the top of each column. The same wing width is used for each temperature in each cell.

for the band's weakest line). Stronger lines, with broader widths, are generally covered by a factor of several more than this. One exception to this rule occurs when calculating water vapor in the far IR/microwave (10–166 cm^{-1}) where the number of spectral lines and narrow line widths (down to 10^{-8} cm^{-1}) preclude an accurate accounting of each line. Rather, in this band, we fix the measurement spacing to 10^{-6} cm^{-1}, though we see negligible effects in our heating rates by making this approximation.

[29] A word about isotopes is warranted here. For carbon dioxide and other gases, numerous isotopologues will typically be found in the atmosphere. In many cases, these rare isotopes may have as many (or more) identified spectral lines as the dominant (primary) isotope, although their abundance may be several orders of magnitude less than the primary. Carbon dioxide, for example, has eight identified isotopes within HITRAN, although the primary isotope comprises, on Earth, ~98.4% of all CO_2 in the atmosphere. By incorporating the additional spectral lines of the isotopologues, we increase the computational time required by a factor of several, and gain only a small improvement in accuracy in our heating rates, since the overall abundance of the rare isotopologues is so low. The negligible influence of the lesser isotopes was expressly demonstrated by *Halevy et al.* [2009]. For this reason, we neglect all but the primary isotope of CO_2 (the '626' isotope) in our calculations. We likewise use only the primary isotope of H_2O (the '161' isotope), which accounts for 99.7% of all H_2O abundance on Earth, and a roughly similar value on Mars.

[30] The result of this step is an unsorted, raw spectrum of the type seen in Figure 1a, spanning the 14 bands, with absorption coefficients stored as a function of wavelength.

3.3. Lineshape Modification

[31] The standard Voigt line shape function provides a reasonable, but not exact, representation of line absorption. At various distances from each line center, a particular line shape may be markedly sub- or super-Lorentzian (a line shape more or less rapidly falling off away from center than a Lorentzian profile, respectively), thus by applying the Voigt lineshape only, one may under- or overestimate the true amount of absorption by the line. Additionally, the shape of each line must be adjusted for its inherent asymmetry and for the inclusion of molecular interactions that produce absorption in otherwise "forbidden" wavelengths. These modifications will vary for each of the various potential species in the LUT. Let us briefly describe these adjustments for gases in the Martian atmosphere. A more comprehensive discussion of these adjustments is also found in *Halevy et al.* [2009].

3.3.1. Carbon Dioxide

[32] Carbon dioxide spectral lines are noticeably sub-Lorentzian far from the line center, thus the Voigt line shape in the far wings of a line centered at wavelength ν_0 is corrected by applying a sub-Lorentzian 'chi' scaling factor $\chi(\nu - \nu_0)$. We choose to follow the suggestion in *Wordsworth et al.* [2010], and apply the empirical scaling factor found in *Perrin and Hartmann* [1989] which is used to reduce the line strength in the wings of each CO_2 line beyond 3 cm^{-1} from the line center.

[33] Additionally, each CO_2 line is adjusted by a so-called normalization factor, φ, which accounts for the asymmetry between absorption at frequencies higher and lower than the line center [*Van Vleck and Huber*, 1977]

$$\varphi(v, v_0) = \frac{v \tanh\left(\frac{hv}{2k_B T}\right)}{v_0 \tanh\left(\frac{hv_0}{2k_B T}\right)} \tag{10}$$

The normalization adjustment is incorporated in the form suggested by *Halevy et al.* [2009]. For carbon dioxide, these are the only adjustments we incorporate to modify individual lineshapes. However, the inclusion of various collision-induced absorption bands is also necessary. These once-neglected components of the absorption spectrum arise from the creation and interaction of CO_2-CO_2 dimers and the establishment of previously forbidden transitions that are possible due to strong collisions [*Gruszka and Borysow*, 1997]. Empirical parameterizations of their effects have been developed, although such collision-induced absorption effects remain the major source of uncertainty at high pressures. For carbon dioxide atmospheres, we apply the work of *Baranov et al.* [2004] and *Gruszka and Borysow* [1997] to represent the collision-induced and dimer absorption bands of CO_2 from 0 to 250 cm^{-1} and 1200–1500 cm^{-1}, respectively, again following the suggestion of *Wordsworth et al.* [2010].

3.3.2. Water Vapor

[34] For water vapor, different adjustments to the line shape are implemented, and we follow a scheme discussed in *Halevy et al.* [2009]. For water vapor, the Van Vleck-Weisskopf line shape

$$f_{VVW}(v, v_0) = \left(\frac{v}{v_0}\right)^2 (f_L(v, v_0) + f_L(v, -v_0)), \tag{11}$$

is used in lieu of the Voigt line shape in the far wings (beyond 40 Doppler halfwidths) [*Van Vleck and Weisskopf*, 1945]. In equation (11), f_L represents the pure Lorentz lineshape. This adjustment is especially significant in the microwave region, where water has many lines, but CO_2 is largely transparent. This line shape becomes equivalent to the Lorentz line shape at higher frequencies. As with CO_2, all lines are also modified by the normalization factor in equation (10).

[35] For scenarios where water vapor will be present in our LUT, we apply the MT_CKD continuum code to generate both self- and foreign-broadened water vapor continuum values. This code package, developed at AER, Inc., is a widely used means of representing the water vapor continuum [*Clough et al.*, 2005]. It is designed to quantify the amount of absorption from line wings >25 cm^{-1} from the line center and, as such, we truncate calculations of all water vapor wings at this distance to avoid 'double-counting' of the line wings. Standard output from the MT_CKD is at 10 cm^{-1} resolution, and is temperature dependent. We have prepared a separate look-up table of this data from 0 to 10,000 cm^{-1} every 10 cm^{-1} with 50 K temperature spacing, from 50 K to 400 K. The water vapor IR spectrum is augmented by both the self and foreign continuum values within this spectral range using a bilinear interpolation scheme in wavelength and temperature. Further discussion on the water vapor continuum is deferred until section 4.2.3.3.

3.3.3. Other Gases

[36] Much less is known about other gases that may be found in the Martian atmosphere in trace amounts. For all

other trace species, we apply equation (10) and the Van Vleck-Weisskopf line shape (equation (11)) in the far wings, following the same approach as for water vapor. The width of the line wings extends in the same fashion as for CO_2 (i.e., Figure 2) as there is no empirical calculation of trace gas continua as for water vapor.

3.4. Producing the Spectrum

[37] The aforementioned adjustments to the individual spectral lines leave us now with n individual spectra for the n independent gases (and/or isotopologues) we are modeling, each discretized on the same wavelength grid with a step of $\Delta\nu$. Continuum features are, likewise, discretized on the same grid. For a CO_2-only atmosphere, the absorption coefficient k_{ν_0} at ν_0, then, is simply the sum of the absorption coefficients at ν_0 from lines of the gas within x wave numbers of ν_0 (where x follows Figure 2) plus the CO_2 'continuum' term

$$k_{\nu_0} = q_{CO_2}\left(k_{cont} + \sum_{|\nu-\nu_0|<x}(k_\nu)\right). \tag{12}$$

For a pure CO_2 atmosphere, the CO_2 mixing ratio, q_{CO2}, is unity. In practice, we set q_{CO2} to 0.953 and implicitly assume the remaining atmosphere is comprised of optically transparent N_2. The k-values calculated in sections 3.2 and 3.3, however, are independent of our choice of q_{CO2} and the user may scale these coefficients by any value for q_{CO2} deemed appropriate. Any value of ν_0 in our discretized grid may or may not coincide with a line center. Some may fall very close to or within the core of a single line, but others may fall at a wavelength far from any nearby lines. The value of k_{ν_0} may thus be dominated by a nearby line, or through the collective incremental contributions of nearby line wings. At the edges of each of our 14 spectral bands, we allow for the contributions of wings from lines that fall outside of the spectral band, but within the chosen line wing cutoff value. Thus, for wavelengths near the edges of individual spectral bands, contributions to k_{ν_0} may come from spectral lines falling outside the band edges. These lines must be properly accounted for in the development of the spectral code to avoid underestimating absorption near band edges. In this approach, the only elements of the CO_2 'continuum' are the collision-induced and dimer absorption terms that have been empirically calculated (see section 3.3.1).

[38] For a CO_2-H_2O atmosphere, the overall absorption coefficient is modified to further incorporate the self and foreign continuum values for the water vapor along with the individual water vapor line contributions within 25 cm^{-1}

$$\begin{aligned} k_{\nu_0} = {} & q_{CO_2}\left(k_{cont} + \sum_{|\nu-\nu_0|<x}(k_\nu)\right) \\ & + q_{H_2O}\left(\sum_{\substack{|\nu-\nu_0|<\\ 25\mathrm{cm}^{-1}}}(k_\nu) + \left[\left(\frac{q_{H_2O}p}{p_{ref}}\right)\left(\frac{T_{ref}}{T}\right)k_{HSC}\right.\right. \\ & \left.\left. + \left(\frac{(1-q_{H_2O})p}{p_{ref}}\right)\left(\frac{T_{ref}}{T}\right)k_{HFC}\right]\right), \end{aligned} \tag{13}$$

where in both cases, the q terms represent the mixing ratio of the indicated gas, k_{cont} is the 'continuum' absorption of CO_2 mentioned above and 'k_{HSC}' and 'k_{HFC}' represent the empirically determined H_2O self and foreign continuum coefficients, respectively, at STP, the conditions of p_{ref} and T_{ref}. The latter two terms are scaled to the local (p, T) conditions as shown. Additional absorbing gases, i, can be added to the overall absorption coefficient in equation (13) through simple addition of the product $q_i\Sigma k_i$ as we do not consider their continuum effects. Recall that absorption coefficients are calculated for all gases on the same fine spectral grid, so the summing of multiple gases on the same wavelength grid is straightforward.

[39] At this stage, we have generated a full, high-resolution spectrum of perhaps tens of millions of points for our mixture of gases in our chosen band and at our selected temperature and pressure. But to gain the benefits of the KDM approach, we must now convert this complex spectrum into a simple form, following the path laid out in equations (1) and (2).

3.5. Sorting the Spectrum

[40] Generating a set of representative k-coefficients from the high-resolution spectrum is, itself, a relatively straightforward process. In practice, it requires sorting the discrete k values calculated above by strength (at the same time discarding the spectral information), and identifying a set of weighted points which, when summed together, will reflect the total absorption within the band. To this end, we apply the 'quicksort' algorithm of *Press et al.* [1996] to generate a sorted spectrum (Figure 1b). Spacing between each point within cumulative probability space is the reciprocal of the number of discrete points in the band.

3.6. Gaussian Quadrature

[41] A standard Gaussian quadrature method, such as that found in *Press et al.* [1996] is used to establish the quadrature weights across the distribution—they are not arbitrarily chosen. The corresponding k values that fall at these weights are used to precisely represent the entire distribution. A list of the 32 points in the quadrature are listed in Table 2.

[42] Experience has shown that the visible and IR spectra can be accurately reproduced by 32 quadrature points, and produces results better than prior implementations that use 16 quadrature points. Within each band, the curve is fit with these 32 points at discrete locations along the distribution—16 points between [0–0.95], and 16 points between [0.95–1.0]. These intervals were selected because experimentation has shown that the strongest, and generally most significant absorption occurs at the cores of the individual spectral lines, which are found at the upper end of the distribution. Thus a spectral band, comprised of perhaps as many as 10 million individual k values, can be very accurately represented by 32 terms (k_i) and their corresponding weights (a_i). These values are then used to discretely solve for equation (2) by:

$$Tr = \sum_{i=1}^{32} a_i e^{-k_i u} \tag{14}$$

Table 2. Bin Widths and Cumulative Probability for the 32-Point Gaussian Quadrature Used in the KDM Model

Bin Number	Bin Width	Cumulative Probability
1	0.012897	0.0050346
2	0.029570	0.0263269
3	0.045200	0.0638252
4	0.059199	0.1161829
5	0.071058	0.1815088
6	0.080349	0.2574420
7	0.086737	0.3412383
8	0.089989	0.4298691
9	0.089989	0.5201309
10	0.086737	0.6087617
11	0.080349	0.6925580
12	0.071058	0.7684912
13	0.059199	0.8338171
14	0.045200	0.8861748
15	0.029570	0.9236731
16	0.012897	0.9449654
17	0.0006788	0.9502650
18	0.0015563	0.9513856
19	0.0023789	0.9533592
20	0.0031157	0.9561149
21	0.0037399	0.9595531
22	0.0042289	0.9635496
23	0.0045651	0.9679599
24	0.0047363	0.9726247
25	0.0047363	0.9773753
26	0.0045651	0.9820401
27	0.0042289	0.9864504
28	0.0037399	0.9904469
29	0.0031157	0.9938851
30	0.0023789	0.9966408
31	0.0015563	0.9986144
32	0.0006788	0.9997350

Equation (14) can then be seamlessly incorporated into a standard flux solver to generate atmospheric heating rates.

4. Model Validation

[43] One intent of the present work is to provide a comprehensive validation and proof-of-concept from start to finish of a fast and accurate Mars radiative transfer model. Despite years of work in this area, there has yet to be a thorough discussion of the *k*-distribution approach for Martian conditions in the published literature. While we shall see that these models, in general, perform admirably, it is nonetheless valuable to establish a series of reference conditions over which contemporary and future models can be compared. A significant fraction of Mars atmospheric studies are concerned with the present-day atmosphere, with a relatively simple CO_2 composition (setting aside the question of aerosols for the moment). It is not guaranteed that models appropriate for the present-day will perform equally well when faced with more complex gas mixtures and higher pressures such as those potentially found early in its history. We can, however, test the performance of these models relative to well-established terrestrial standards and to each other, which provides confidence that our model results are reasonably robust. This validation process is an important step in the establishment of a radiative transfer model and, as we shall see, not all models perform equally well.

[44] The KDM model, as fully implemented in a GCM consists separately of a model 'core', or flux solver, which calculates the upward and downward fluxes at discrete atmospheric levels, and the set of absorption coefficients generated in section 3, which define layer opacity for selected atmospheric conditions. As a means of validating the KDM model, both flux solver and *k*-coefficients, and demonstrating its utility for a broad range of atmospheric conditions and compositions, we have produced results in a 1-D atmospheric column model for a number of simplified, prescribed conditions. We compare to the KDM model results from a range of other, commonly used radiative transfer model cores and coefficients including a similar 1-D *k*-distribution radiative transfer model developed at NASA Ames, hereafter referred to as the 'Ames model', the TWOSTR two-stream algorithm based on the DISORT discrete ordinances model [*Kylling et al.*, 1995], (the 'TWOSTR model'), a *k*-distribution approach first developed by *Kasting et al.* [1984] and subsequently employed elsewhere [*Kasting*, 1991; *Pavlov et al.*, 2000; *Haqq-Misra et al.*, 2008] (the 'Kasting model'), a simplified band model approach for the Martian atmosphere used in an earlier version of the LMD Mars GCM [*Forget et al.*, 1999], (the 'wideband model') and a line-by-line approach, LBLRTM, [*Clough et al.*, 1992, 2005] developed by AER, Inc. (the 'LBLRTM model').

4.1. Model Descriptions

[45] The KDM flux solver is a variant of the approach described by *Edwards and Slingo* [1996]. Fluxes are solved for at each model level in the upward and downward direction, and net fluxes derived from these components. Conversion of the flux divergence ($\Delta F/\Delta p$) between two model levels into a heating rate ($\Delta T/\Delta t$) of a model layer is solved simply as

$$\frac{\Delta T}{\Delta t} = \frac{\Delta F}{\Delta p}\frac{g}{c_p}, \tag{15}$$

where c_p is the specific heat of the atmosphere for fixed pressure (temperature-dependent), and g is the gravity at Mars (3.72 ms^{-2}).

[46] We have obtained both the Ames model core and absorption coefficients from the Ames Mars climate modeling group through their publicly accessible website at (http://spacescience.arc.nasa.gov/mars-climate-modeling-group/code_form.html). The Ames radiative transfer model, derived from *Toon et al.* [1989] is a generalized two-stream approximation and is used with the Ames Mars GCM. It has been used in a variety of present and past Mars simulations. It employs a similar approach to generating *k*-coefficients as the KDM, but consists of 12 spectral bands (5 IR/7 visible), and has significantly larger (p/T) spacing than our KDM (ΔT = 50 K, $\Delta\log(p)$ = 1.0). Furthermore, it uses a 16-term quadrature compared to the 32-terms of the KDM.

[47] We have obtained the DISORT/TWOSTR-based solver as an additional model core for comparative testing. TWOSTR is a two-stream algorithm for radiative transfer in vertically inhomogeneous, non-isothermal atmospheres [*Kylling et al.*, 1995] that has seen wide usage in the atmospheric science community and has well validated and tested against a wide range of solutions. It uses the eigenvalue decomposition method (often called the 'discrete ordinate' method) discussed in *Kylling et al.* [1995].

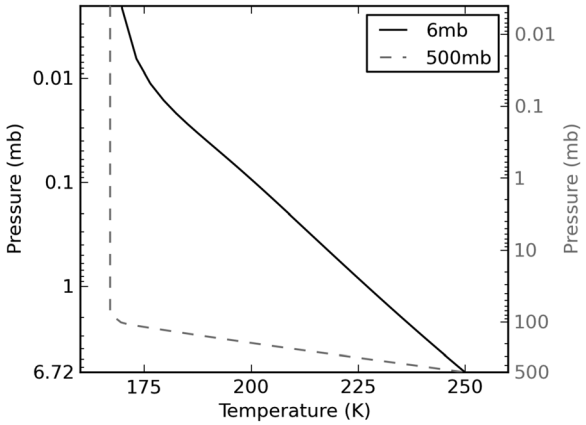

Figure 3. Temperature profiles used for both present-day (black, solid curve) and early (gray, dashed curve) Mars (also see Appendix A).

[48] Among the KDM, Ames and TWOSTR models, we have available to us three distinct flux solvers and two independent sets of *k*-coefficients, for a total of six possible arrangements. We have created a front-end 'wrapper' around the three model cores that allows us to incorporate either set of absorption coefficients with any of the three flux solvers. Results from cross-testing combinations of these model cores and absorption coefficients will highlight any potential issues with the individual cores and, separately, any issues with the two sets of *k*-coefficients.

[49] Results from the Kasting model for these four profiles were obtained directly from the Kasting research group at The Pennsylvania State University. The Kasting model is also a *k*-distribution model, and handles both water vapor and carbon dioxide, using 6 terms in the visible wavelengths and 8 terms in the IR. A description of this model may be found in *Pavlov et al.* [2000] and *Haqq-Misra et al.* [2008].

[50] Results of the wideband model are based on an implementation of the shortwave heating rate solution provided in *Forget et al.* [1999] and a wide-band approach to 15 μm IR cooling from *Hourdin* [1992]. In the visible spectrum, the wideband model does not calculate layer fluxes; rather, the heating rate at each layer is empirically determined. Thus, visible fluxes will not be shown in our validation tests of the wideband model. In the infrared, the *Hourdin* [1992] approach considers only fluxes between 500 and 865 cm^{-1}, assuming the remainder of the IR region to be transparent. To provide a comparison to the other approaches, we have calculated the blackbody radiation of the 250 K surface used in our standard tests from 0 to 500 cm^{-1} and 865–2222 cm^{-1} (the limits of our IR region) and added this value, 135.86 W/m^2, to the calculated 15 μm band fluxes at each level. The wideband model does not account for collision-induced or dimer absorption, and does not account for water vapor or other gases.

[51] As an additional comparison, we have incorporated LBLRTM as a 'standard', high-accuracy line-by-line approach with which to validate the other approaches. Spectral lines in the IR are obtained using the AER code LNFL for the 0–2000 cm^{-1} region (LBLRTM is restricted to spectral bands of $\leq$2000 cm^{-1}), which are ingested into LBLRTM. Output from LBLRTM is fed into the AER code RADSUM, which produces layer fluxes that can be directly compared to the other models. We have adjusted LBLRTM to account for the different physical properties of Mars versus Earth, including planetary radius, specific heat of the atmosphere and gravity. Because of the 2000 cm^{-1} limitation on LBLRTM, it becomes challenging to properly model the visible spectrum (which spans $\sim$40,000 cm^{-1}), and we do not include fluxes or heating rates for the visible portion of the spectrum in this validation.

[52] All models are run in the same general 1-D framework, and consist of 100 model layers bounded by 101 levels, with the lowest level corresponding to the surface. The visible surface albedo is set to 0.2, and IR emissivity assumed to be unity. A pre-determined temperature and water vapor profile (Figures 3 and 4 and Appendix A) is assigned to the middle of each model layer, and each model level is assigned a pressure value.

[53] As a test of the limits of these approaches for both present-day and early Mars, we have conducted four standard tests, two for the present-day ($\sim$6 mb surface pressure) both with and without atmospheric water vapor, and two for a putative early Mars condition having a faint young Sun [*Gough*, 1981; *Sackmann and Boothroyd*, 2003] of 75% present-day luminosity ($\sim$500 mb surface pressure), also both with and without water vapor. Results from these four tests can be found in Figures 5–8 for the various profiles and are further discussed below.

4.2. Results

4.2.1. Present-Day Conditions

[54] On present-day Mars, the atmosphere is predominantly CO_2, with a mean surface pressure of 6–10 mb. Trace amounts of water vapor are present, but in quantities not capable of significantly modifying the atmospheric temperature. We use a simple monotonic temperature profile in the troposphere, with a stratospheric temperature of 168 K for our present-day tests (Figure 3 and Appendix A). Figures 5 and 6 compare the fluxes (upwards and downward) for the various models using this temperature profile, with and without atmospheric water vapor, respectively.

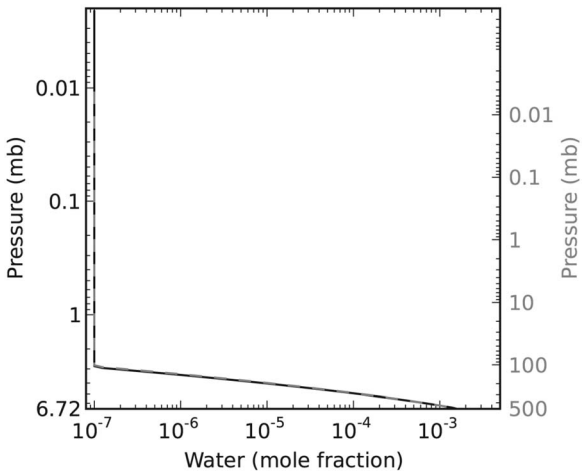

Figure 4. Water vapor profile used in the water vapor simulations for present-day and early Mars (also see Appendix A).

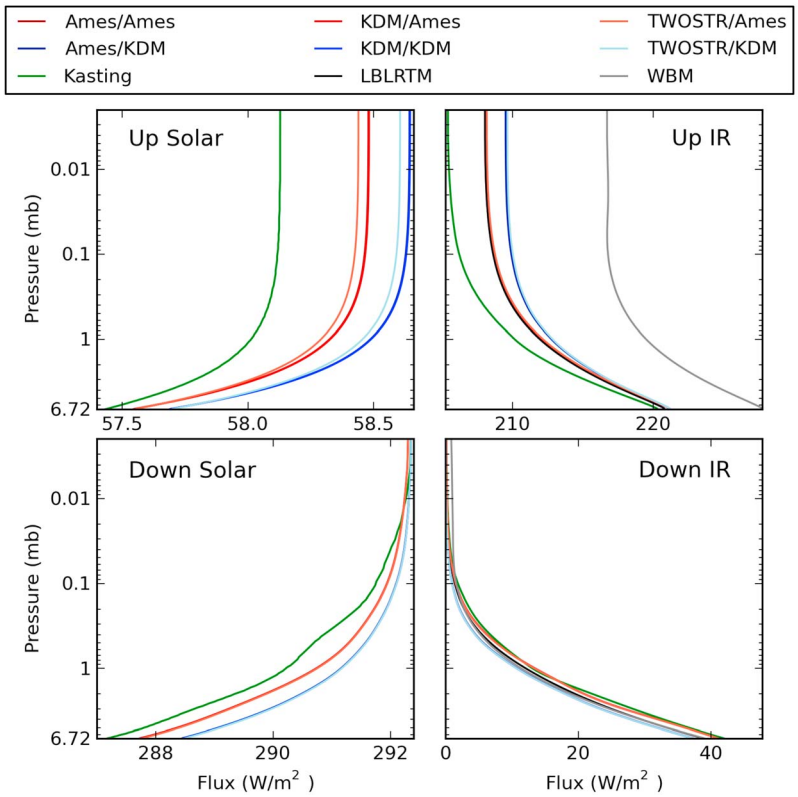

Figure 5. (left) Visible and (right) IR fluxes in a 6 mb CO_2-only atmosphere. (top) Upward fluxes; (bottom) downward fluxes. Legend nomenclature describes models as listed in the text. Where appropriate, prefix in the name refers to the model core used and suffix refers to *k*-table employed.

[55] Based on the results, one can essentially segregate the models into two groups with two outliers. Some sets of curves overlap quite closely (e.g., red/pink/burgundy or light blue/dark blue/purple). These results represent use of the same absorption coefficients with each of the three different flux solvers (KDM/Ames/TWOSTR). The small differences between these two curve sets, red and blue, represent inherent differences that must exist between the two absorption coefficient tables (had the differences segregated according to flux solver, this would have indicated substantive differences among solvers, which is not the case). Differences in layer fluxes are nominal between the KDM/Ames/TWOSTR solutions using the same absorption coefficients, indicating that all three model cores perform the same and, notably, the KDM core performs as expected. Differences between those results for the Ames coefficient group and the KDM coefficient group are <0.5% in both solar and IR wavelengths. These differences are likely attributable to the numerous slight differences in the approaches taken in developing the absorption coefficients tables. Choices such as which isotopologues are incorporated, line cutoff, number of bands and quadrature terms, etc. will cause compounded differences in the final solutions.

[56] The Kasting and wideband models deviate somewhat noticeably from the other results. The Kasting model is reasonably close to the other approaches, but tends to be slightly too absorbing for the downward solar stream and for the upward IR stream. Differences in layer fluxes compared to the LBLRTM standard (in the IR) are <1%, and fluxes in the visible wavelengths differ by 1–2 W/m^2 from the KDM/Ames/TWOSTR groups.

[57] The wideband model is substantially different in the IR, and produces an excess of blackbody emission of ~228 W/m^2 from a 250 K surface compared with the expected blackbody value of ~221 W/m^2 seen in the other runs. As stated before, fluxes are not produced by the wideband model in the visible wavelengths, and are not shown.

[58] Similar results (Figure 6) including a saturated water vapor profile show only very slight variations from Figure 5, which confirms the insignificance of water vapor for current Martian conditions, with variations in fluxes by no more than a few W/m^2 at all heights.

4.2.2. Early Mars Conditions

[59] For early Mars, we assume a predominantly CO_2 composition with a surface pressure of 500 mb. As the water vapor content is also unknown, we frame the potential atmospheric states by using dry and water-rich end-members. The temperature profile used is different from the present-day [*Kasting* 1991; *Mischna et al.*, 2000], and is also shown in Figure 3. Solar flux is set to 75% of the present-day value to accommodate the faint young Sun. The approach taken for these tests is the same as for the present-day, and Figures 7 and 8 compare fluxes for the various models as before.

[60] At higher pressures, we begin to see a greater departure from the LBLRTM standard for the wideband model, which is tuned to present-day conditions, and this performance was not wholly unexpected. Errors >10% are seen in the water-free 500 mb atmosphere and in excess of 25%

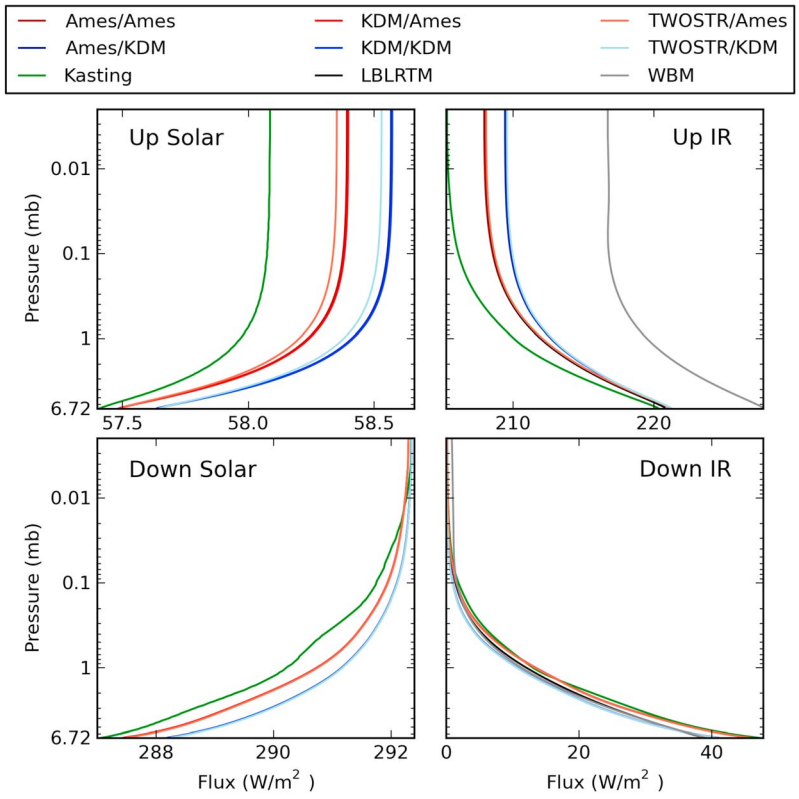

Figure 6. Same as Figure 5, but with a water vapor profile as shown in Figure 3.

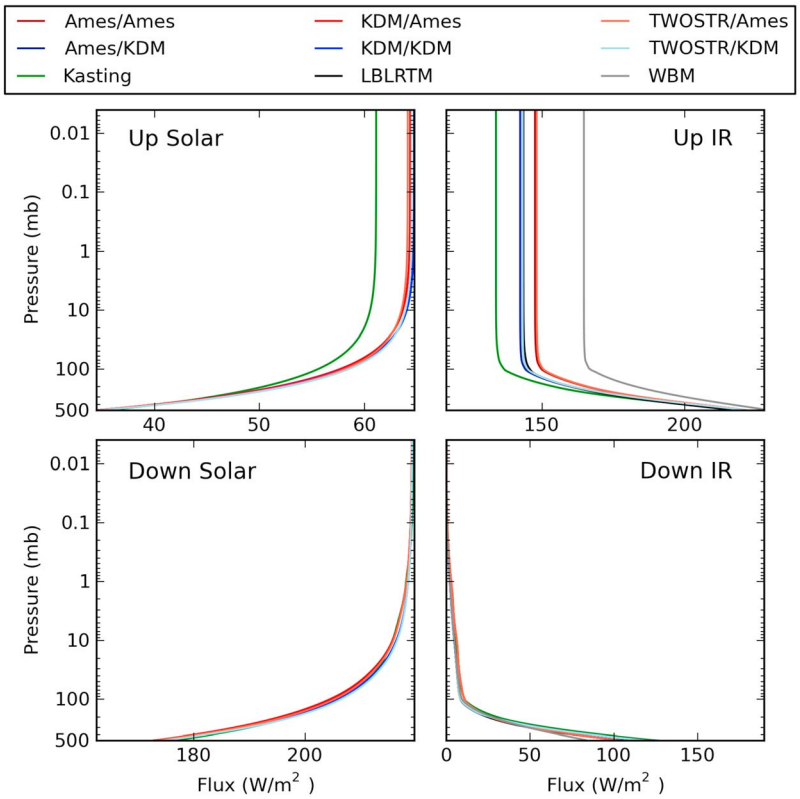

Figure 7. (left) Visible and (right) IR fluxes in a 500 mb CO_2-only atmosphere. (top) Upward fluxes; (bottom) downward fluxes. Legend nomenclature describes models as listed in the text.

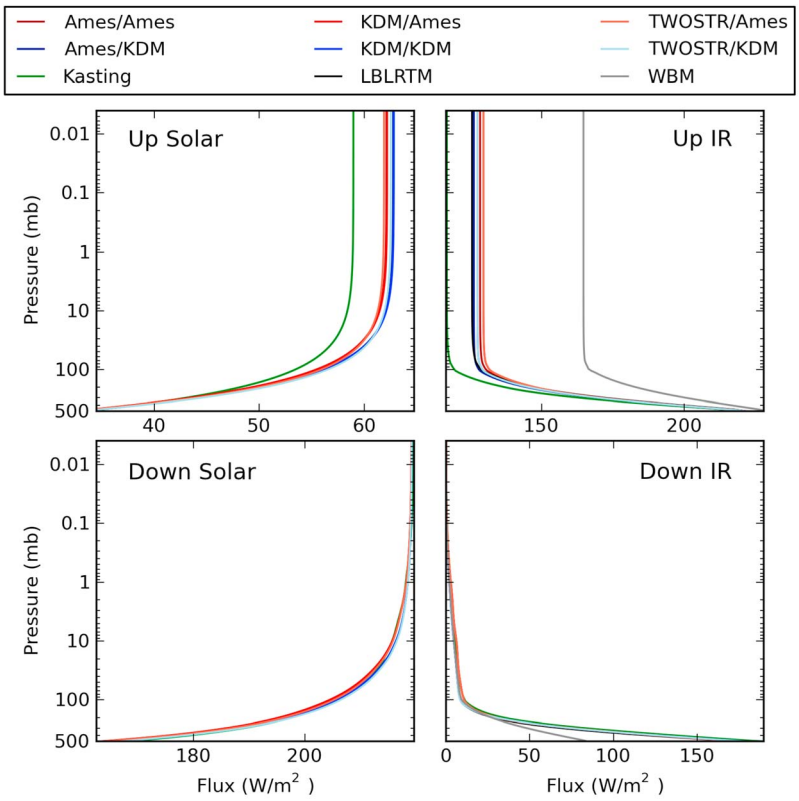

Figure 8. Same as Figure 7, but with a water vapor profile as shown in Figure 3.

when water is included. The Kasting model also departs from the standard by ~5%—far less than the wideband model, but substantially worse than the KDM/Ames/TWOSTR models which all fall within a couple W/m^2 of the others.

[61] A look at heating rates (Figure 9) reflects the goodness of fit of the flux curves above to the standard. In all four cases, all models perform reasonably well in the lower atmosphere, and begin to diverge above about 1 mb. Heating rates calculated using the KDM scheme match fairly well to LBLRTM at present, and very well for the early Mars, high-pressure conditions. They are quite good in the IR in all circumstances, and deviate slightly, at low pressures, in the visible wavelengths. In all cases, the KDM model has slightly lower heating/cooling rates than the corresponding Ames model, both of which straddle LBLRTM.

[62] Conditions on early Mars may have been somewhat warmer at the surface than shown in our test cases, and Figure 10 shows upward IR fluxes for surface temperatures of 275 K (solid lines) and 290 K (dashed lines), respectively (cf. Figure 8, at a surface temperature of 250 K). For both conditions in Figure 10, the atmosphere is saturated at all levels. For ease of viewing, we have shown only results using the KDM flux solver, since it was previously shown that the three flux solvers provide similar results. The same general trends are observed as at 250 K, with a very slight increase in separation between simulations using KDM and Ames coefficients with increasing temperature. As before, both the Kasting and WBM models appear as outliers of modest (Kasting) and progressively worse (WBM) deviation. Overall, the KDM scheme performs quite well.

4.2.3. Sensitivity Studies

4.2.3.1. Band Selection

[63] Our choice of using 14 bands, and, more specifically, 7 in the IR is a departure from other *k*-distribution approaches, such as the Ames model, which use 5 bands in the IR. The difference is in our approach to modeling the 15 μm CO_2 absorption band, where our approach partitions this region into three distinct bands instead of one. How sensitive are these results to the incorporation of these two additional bands, and is the added benefit worth the additional computational cost? We demonstrate, using the same 6 mb and 500 mb water-free atmospheres as in the previous section, the consequence of increasing spectral resolution in this important region.

[64] Figure 11 shows the negligible change in directional fluxes introduced by the addition of these two bands for the present-day atmosphere. All three curves in each panel use the KDM core with different *k*-tables. The green curve uses a 12-band version of the KDM table (in which the three 15 μm bands are combined into a single band, cf. Table 2), and may be compared to the red curve, which is the standard 14-band version of the KDM table. For comparison, the Ames table (also 12 bands) is shown in black. The similarity between red and green curves shows there is little gain in incorporating two additional bands.

[65] The scenario is different, however, at higher pressures where, in Figure 12, we see a noticeable shift in position of the green curve, again representing our 12-band KDM table. Under these circumstances, the 12-band KDM table behaves much more like the 12-band Ames table, and there is an observable difference of about 3 W/m^2 gained at all levels by

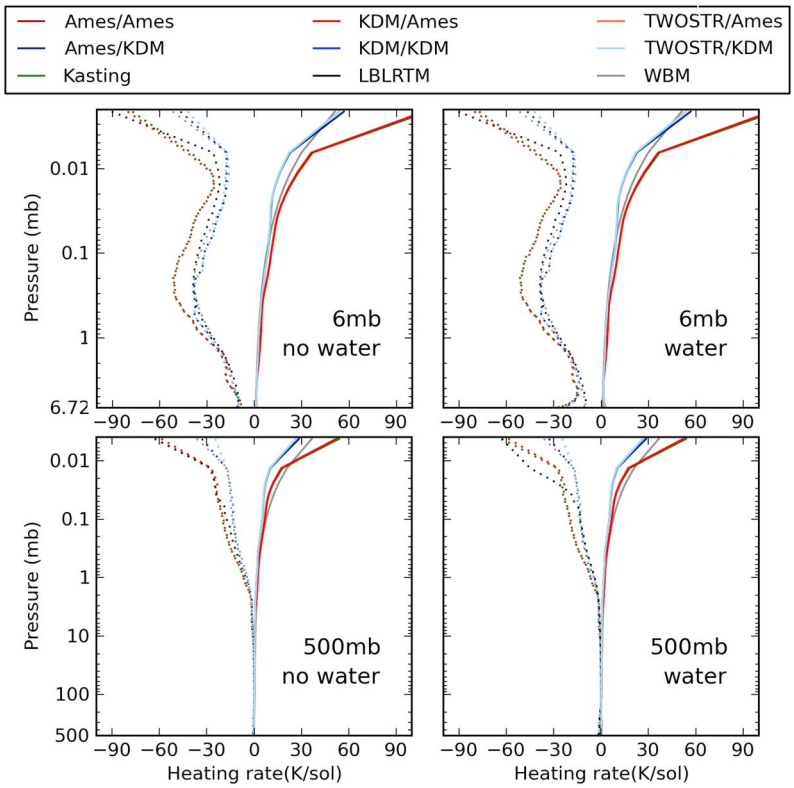

Figure 9. Heating (solid) and cooling (dotted) rates for the nine models tested, for the four simulated conditions shown in Figures 5–8.

including additional bands. This is a consequence of the greater absorption imparted in the 15 μm band wings (KDM IR bands 3 and 5) at higher pressure. As absorption becomes more significant in these bands, the assumption that the Planck curve is approximately constant between 416 and 833 cm^{-1} begins to break down, and a finer partitioning of the 15 μm region becomes more important. The impact in heating rates, while apparently small in the lower atmosphere for these idealized profiles, can become significant in the middle atmosphere.

4.2.3.2. The k-Table Density

[66] The spacing between adjacent coefficients in the respective *k*-tables also differs between implementations. How significant is the choice of spacing in temperature and pressure? We briefly address this issue here. Relative to our 'baseline' spacing of 20 K and 0.4 log(p), we compare results with double (40 K and 0.8) and triple (60 K and 1.2) spacing in both terms. The change in atmospheric heating rate resulting from a change in *k*-table density is shown in Figure 13 for present-day Mars.

[67] Examination of the IR (cooling) rate profiles shows an increase in oscillatory behavior in the profile as spacing increases. Studying the points at which the oscillation amplitude maxima occur shows them to be most pronounced at levels for which the interpolation distance in T and/or p is at a maximum (i.e., 30 K and 0.6 log(p) for the coarsest 60 K/1.2 spacing). At certain locations (e.g., ~0.1 mb in Figure 13, where the local temperature T = 200 K falls between coarse table values at 170 K and 230 K and 0.06 mb and 1 mb), heating rates can vary by as much as 50% compared to the finer grid mesh (compare the black and green curves). The same behavior has been observed in other, comparable, tests. The error introduced cannot be readily predicted a priori as it

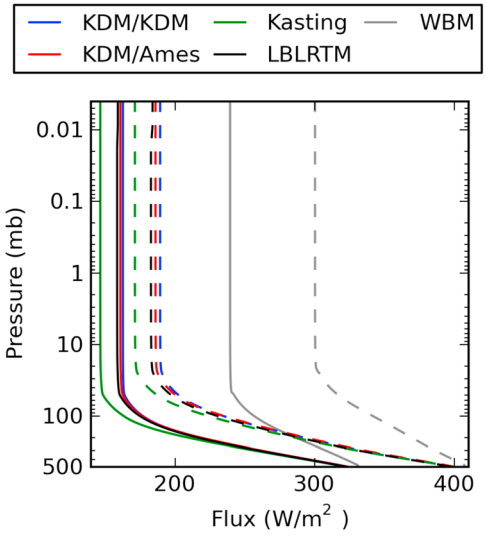

Figure 10. Upward IR fluxes for five different models with a saturated atmosphere and surface temperature of 275 K (solid lines) and 290 K (dashed lines) in a 500 mb atmosphere.

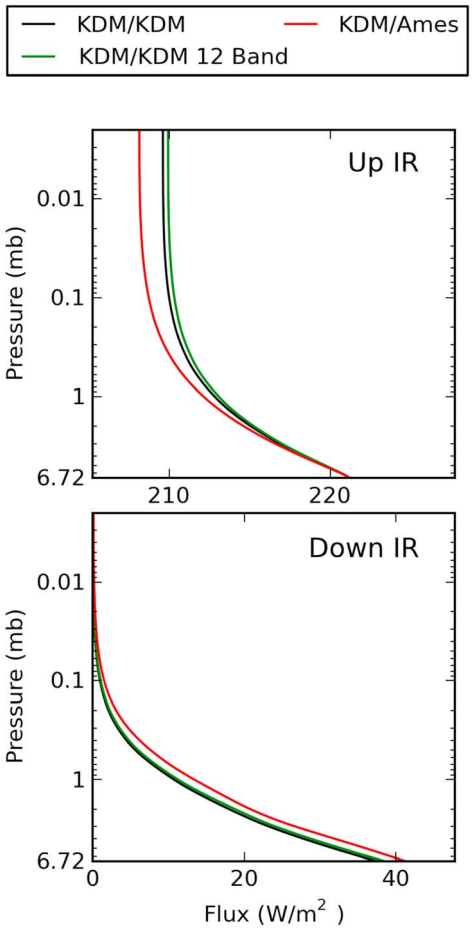

Figure 11. Directional IR fluxes for three different implementations of the 15 μm CO_2 band for present-day atmosphere. All implementations use the KDM flux solver. Black curve: Ames 12-band *k*-table (1 band spanning 15 μm region); Red curve: KDM 14-band *k*-table (3 bands spanning 15 μm region); Green curve: KDM 12-band *k*-table (1 band spanning 15 μm region).

depends largely on the temperature profile being examined. Regardless, potential errors in atmospheric heating rates are magnified as the table grid spacing increases, and it is apparent that a reduction in table spacing will reduce these types of interpolation errors.

4.2.3.3. Line Shape and Continuum Contributions

[68] By separating some of the individual components that go into developing the spectrum, it is possible to see the relative influence of the choices that are made. One such component is the normalization factor shown in equation (10). The results of omitting the normalization factor completely are shown by the red curves in Figures 14 and 15 for the present-day and early Mars, respectively. On present Mars, the influence is small, less than 0.1 W/m^2. On early Mars, the normalization factor acts to reduce the outgoing IR flux by ~2.5 W/m^2, or about 2%. As noted in *Halevy et al.* [2009], the particular choice of normalization factor (Van Vleck-Huber, linear, quadratic), has a much smaller effect than the use of the factor itself.

[69] The water vapor continuum is a component of the spectrum that is significant, especially for thicker, more humid atmospheres. Generally, the water vapor foreign continuum (k_{HFC} in equation (13)) will dominate over the self-continuum in the Martian atmosphere, which is overwhelmingly CO_2. The magnitude of the contribution of the water vapor foreign continuum is indicated by the green line in Figures 14 and 15 and, as expected, manifests itself in saturated, early Mars conditions, where it reduces the outgoing IR flux by ~4 W/m^2, or about 3%. The self-continuum term will contribute an additional, but substantially smaller contribution, and is not shown.

[70] There is still significant uncertainty in how best to treat the water vapor continuum in a predominantly CO_2 atmosphere, and a few words are warranted here. Continuum models such as MT_CKD are designed for terrestrial compositions and conditions, and are not strictly applicable to those found on Mars. While the self-continuum is probably so small as to be reasonably negligible, the same does not hold for the foreign continuum. Here, many uncertainties in the line shape of water vapor lines, especially in the atmospheric 'window', remain. While CO_2-broadened water vapor line half-widths on Mars may be larger than air-broadened lines on Earth, yielding a somewhat higher

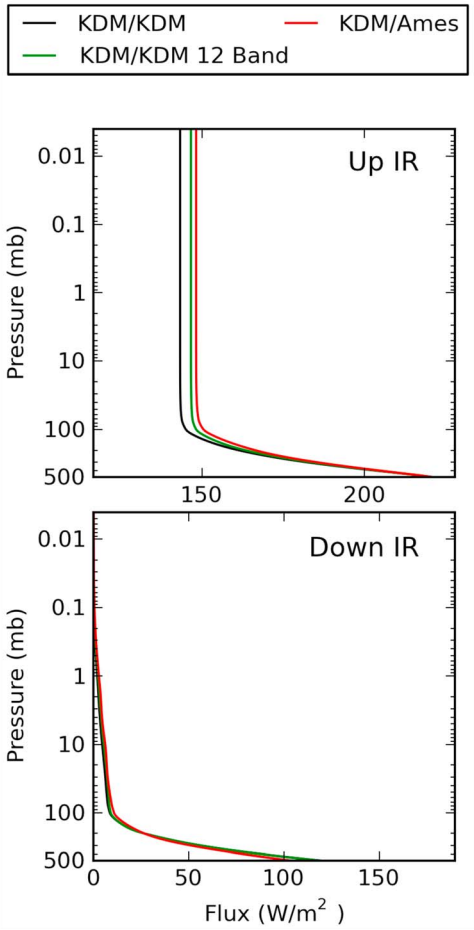

Figure 12. Same as Figure 10, but for 500 mb (early Mars) atmosphere. At higher pressures, inclusion of extra bands in the 15 μm region becomes more significant.

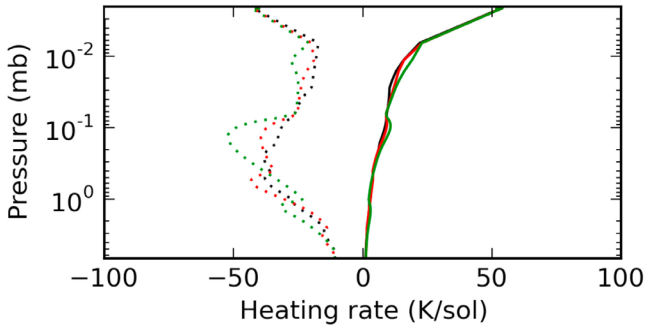

Figure 13. Heating rates for present-day atmosphere with three different *k*-table densities. Black curve: standard table density, with $\Delta T = 20$ K, $\Delta\log(p) = 0.4$; Red curve: doubled spacing ($\Delta T = 40$ K, $\Delta\log(p) = 0.8$); Green curve: tripled spacing ($\Delta T = 60$ K, $\Delta\log(p) = 1.2$). Oscillations in curves reflect the distance over which interpolations must be performed and depend on local (p, T) conditions. Oscillation magnitudes grow as spacing in *k*-table increases, most noticeably in the IR.

continuum absorption in the water vapor bands (near the line centers), the sub-Lorentzian 'chi' line shape factor in the far wings of the water vapor lines in the 'window' may likewise differ, but by an unknown amount and sign. In short, the full line shape, particularly in the sensitive 'window' region of the spectrum, is not fully understood for Mars, and so our choice to use terrestrial-based foreign continuum coefficients represents a reasonable, though likely lower, bound.

[71] Additionally, a second component of the continuum, derived from absorption by induced-dipole interactions between two molecules, differs between CO_2-H_2O and air-H_2O interactions, but to what extent remains uncertain, and thus we likewise employ the air-H_2O values as found in MT_CKD. This, too, is likely a lower bound, but grounded in the available research. Future measurements will be able to more firmly establish suitable water vapor continuum values for CO_2-dominated atmospheres, which can easily be incorporated into the KDM, where we expect to find a small-to-modest increase in atmospheric absorption.

4.2.4. Global Circulation

[72] As a final demonstration of the KDM radiative transfer scheme we show some idealized, but full, 3-D GCM results. The simulations are 'idealized' in the sense that we do not include the radiative effects of dust or ice aerosols. This has been done in order to show the impact of the gas radiative transfer in isolation. As a result, it is inappropriate to compare our current Mars simulations against data. Indeed comparisons with data including aerosol effects would be moot for our purposes in this paper since they provide more insight into the quality of the aerosol heating than they do in to gas heating. As such, these simulations highlight the dynamical consequences of improvements in radiative heating.

[73] As a GCM framework, we employ a 40-layer version of the MarsWRF GCM for all our tests. Details of the model

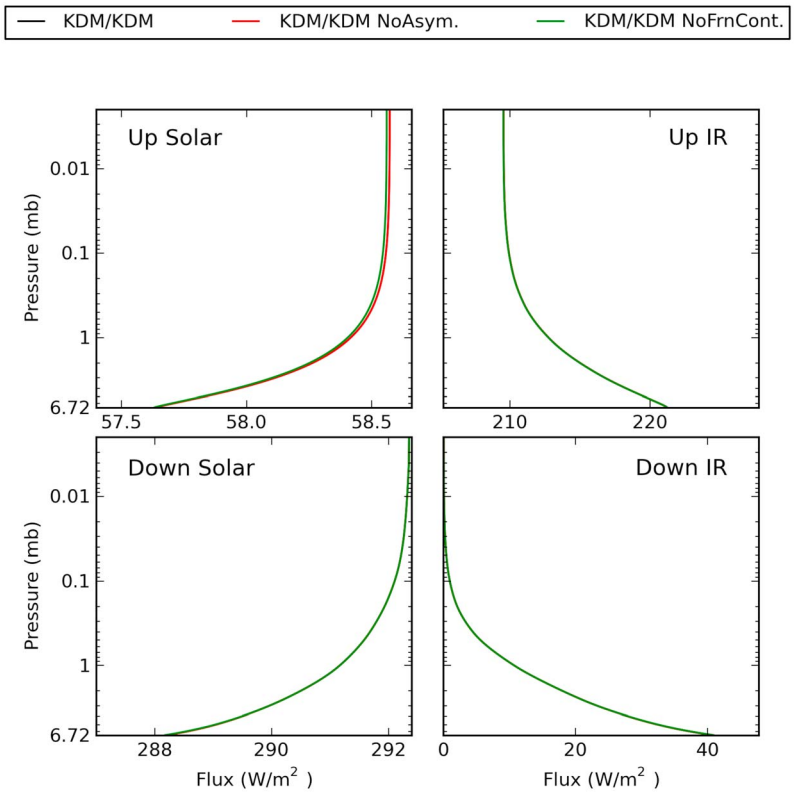

Figure 14. (left) Visible and (right) IR fluxes in a 6 mb CO_2 atmosphere with water vapor. (top) Upward fluxes; (bottom) downward fluxes. Black curve is standard run using the KDM flux solver and KDM k-coefficients. Red curve shows fluxes with normalization factor removed, and green curve shows influence of water vapor foreign continuum (k_{HFC}) on fluxes.

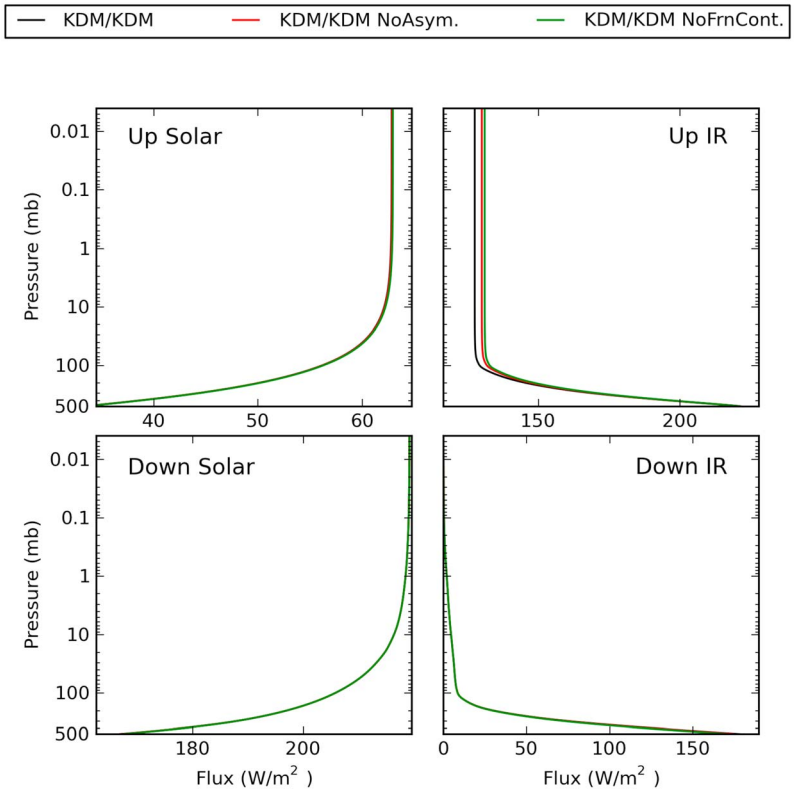

Figure 15. Same as Figure 13, but for 500 mb CO_2 atmosphere with water vapor.

may be found in *Richardson et al.* [2007]. As with the 1-D simulations, we employ a 75% present-day solar luminosity in our 500 mb simulations. Surface albedo and thermal inertia are matched to Mars Global Surveyor Thermal Emission Spectrometer (TES) observations [*Christensen et al.*, 2001; *Putzig et al.*, 2005]. While the model is generally well tuned to present-day observed conditions, the exact details are not important as our simulations all employ the

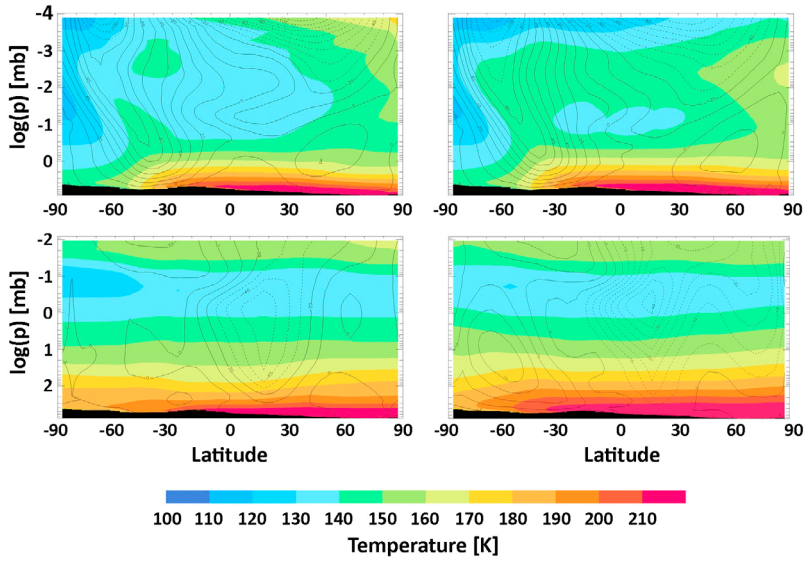

Figure 16. Zonally and temporally averaged vertical slices of the Martian atmosphere from MarsWRF GCM simulations for the time period L_s = 90–120°. (top) Present-day atmosphere; (bottom) early Mars atmosphere. (left) Results using the KDM radiation scheme discussed above; (right) results using the WBM radiation scheme. All simulations have dust-free atmospheres and are otherwise identical. Colors indicate temperature (K) and contours show wind speed (m/s). Solid lines are westerlies, dashed lines are easterlies.

same conditions save for the choice of radiative transfer approach.

[74] We first consider the current atmospheric mass. Figure 16 shows the zonal mean temperature and zonal wind structure for $L_s = 90°–120°$. As expected, the structure of the atmospheres is rather similar between the two cases. The atmosphere is dominated by the strong winter polar front and the associated winter polar vortex, which extends to the model top. In the summer hemisphere, the near surface layers are substantially warmer than the remainder of the atmosphere and at high altitudes above the summer hemisphere a significant easterly flow develops. Slight differences between the cases do occur. The near surface is slightly warmer in the wideband model simulation, and the wideband model atmosphere appears slightly more strongly forced, with a stronger polar jet and stronger adiabatic heating along the polar front. In general, however, the KDM and wideband model cases show qualitatively the same atmospheric state as would be expected from the rather similar performance of these schemes for current Martian atmospheric pressures and temperatures (Figures 5 and 6).

[75] The 500 mb case is beyond the range of validity of the wideband model and is shown here merely to illustrate the degree to which the thermal structure and circulation can easily and irredeemably impacted by errors in radiative forcing for paleoclimate cases. In the southern (winter) hemisphere (these cases are also shown for $L_s = 90°–120°$), the wideband model produces far more cooling, resulting in a colder polar atmosphere and a deeper and stronger polar vortex. Indeed, the KDM scheme creates a split in the polar vortex near 50 mb, with the westerly jet in the lower atmosphere pushed to the lower midlatitudes. Strong westerlies reestablish in the winter hemisphere only above about 5–10 mb. The weak polar jet is associated with flat or even increasing temperatures with increased southern latitude. Over the equator, a much stronger easterly jet is evident with the KDM scheme than with the wideband model. That the wideband model should diverge from the KDM scheme is not surprising given that the wideband model is beyond its range of validity, but it is interesting that the structure and dynamics resulting from its use are so different from the KDM. This highlights the crucial importance of approaches like the KDM that have been validated against LBL calculations for paleoclimate usage in GCMs.

5. Summary

[76] We have presented the mechanics behind a flexible and efficient means of performing radiative transfer calculations in the Martian atmosphere that addresses many of the shortcomings of previous approaches [e.g., *Hourdin*, 1992], and presented a technical framework with which the reader may readily develop a similar scheme. While similar approaches have been used in some recent investigations of CO_2-rich early Martian atmospheres [*Johnson et al.*, 2008; *Halevy et al.*, 2009; *Wordsworth et al.*, 2010], few details have thus far been given that allow accurate comparisons of these models or reproduction of their results for a wide range of past and present Martian conditions, and accurate recreation of the absorption coefficients central to this approach has not been possible. Our goal here was to enable these critical components of scientific investigation in a way that is easily accessible to those who regularly involve Mars GCM studies in their work.

[77] Initial development of the absorption coefficients is the most time consuming step, and, for a two-gas atmosphere (e.g., $CO_2 + H_2O$) requires creation of a 4-D look-up table (with dimensions: pressure, temperature, wavelength band, atmospheric composition) to cover all plausible atmospheric conditions. An absorption spectrum for each pressure/temperature/composition triple is created from HITRAN, and modified to reflect both adjustments to the line shape from the standard Voigt lineshape as well as a parameterization of continuum absorption. The final product is then partitioned into discrete spectral bands where the line intensity curve is sorted by strength and fit using a Gaussian quadrature method with 32 points. These 32 points are the product included in the look-up table, and reflect an orders-of-magnitude faster means of calculating atmospheric absorption than with a line-by-line approach.

[78] The model has been validated against existing approaches, and shows excellent agreement against two standard models currently implemented for present-day conditions as well as line-by-line models. For high pressure atmospheres with both CO_2 and H_2O, departures from these standard models reflect absorption that has been neglected by the standard models, and which has been known to be a shortcoming of these previous approaches. The advantage of the present model is the simplicity with which additional atmospheric species may be incorporated to explore a wide range of putative early Martian climates. The strengths of this approach may be seen in a forthcoming companion paper that addresses the ability of mixed $CO_2 + H_2O + SO_2$ atmospheres to provide periodic warming of the early Martian atmosphere.

Appendix A

[79] Table A1 provides the relevant physical parameters used in the 100-layer models employed in this validation. Sigma values are terrain-following coordinates that reflect the ratio of the local pressure level to the surface pressure ($\sigma = 1.0$ at the surface). Temperature value n reflects the temperature of layer n, which sits between levels n and $n + 1$. Temperatures at level 101 (italicized) are surface temperatures, and coincide with level 101. Water vapor mixing ratio value n likewise reflects value of layer n.

[80] **Acknowledgments.** The authors would like to thank Ramses Ramirez and Jim Kasting for data from their model, and for useful discussions that improved the output of our 1-D model. Also, Karen Cady-Pereira and Eli Mlawer of AER, Inc. who assisted with implementation of the LBLRTM code as well as incorporation of continuum absorption in our line-by-line code. Resources supporting this work were provided by the NASA High-End Computing (HEC) Program through the NASA Advanced Supercomputing (NAS) Division at Ames Research Center as well as from the JPL Office of the Chief Information Officer. M.A.M. and C.L. were supported by a NASA Mars Fundamental Research Program grant NNH10ZDA001N to JPL. Additional support for C.L. and M.I.R. was provided by a NASA Planetary Atmospheres grant NNX10AB42G to Ashima Research. Part of this research was carried out at the Jet Propulsion Laboratory, California Institute of Technology, under a contract with the National Aeronautics and Space Administration. The authors would like to thank two anonymous reviewers for their comments on and suggestions for this manuscript.

Table A1. The Relevant Physical Parameters Used in the 100-Layer Models Employed in This Validation[a]

Level Number	6 mb Sigma	6 mb Temperature	500 mb Sigma	500 mb Temperature	Water Vapor
1	0.007688	168.00	0.000107	167.00	1.00E-07
2	0.008313	171.40	0.000124	167.00	1.00E-07
3	0.008983	174.80	0.000144	167.00	1.00E-07
4	0.009701	178.00	0.000166	167.00	1.00E-07
5	0.010471	181.00	0.000192	167.00	1.00E-07
6	0.011294	183.80	0.000221	167.00	1.00E-07
7	0.012176	186.30	0.000255	167.00	1.00E-07
8	0.013118	188.60	0.000293	167.00	1.00E-07
9	0.014125	190.70	0.000337	167.00	1.00E-07
10	0.015200	192.60	0.000386	167.00	1.00E-07
11	0.016347	194.30	0.000443	167.00	1.00E-07
12	0.017571	196.00	0.000507	167.00	1.00E-07
13	0.018875	197.49	0.000580	167.00	1.00E-07
14	0.020264	198.88	0.000663	167.00	1.00E-07
15	0.021741	200.19	0.000756	167.00	1.00E-07
16	0.023313	201.44	0.000862	167.00	1.00E-07
17	0.024983	202.62	0.000982	167.00	1.00E-07
18	0.026759	203.75	0.001117	167.00	1.00E-07
19	0.028643	204.83	0.001269	167.00	1.00E-07
20	0.030640	205.88	0.001440	167.00	1.00E-07
21	0.032759	206.88	0.001633	167.00	1.00E-07
22	0.035002	207.86	0.001849	167.00	1.00E-07
23	0.037378	208.81	0.002092	167.00	1.00E-07
24	0.039892	209.73	0.002364	167.00	1.00E-07
25	0.042547	210.63	0.002668	167.00	1.00E-07
26	0.045355	211.51	0.003008	167.00	1.00E-07
27	0.048318	212.36	0.003387	167.00	1.00E-07
28	0.051444	213.20	0.003810	167.00	1.00E-07
29	0.054741	214.02	0.004281	167.00	1.00E-07
30	0.058214	214.83	0.004805	167.00	1.00E-07
31	0.061871	215.62	0.005387	167.00	1.00E-07
32	0.065718	216.40	0.006033	167.00	1.00E-07
33	0.069763	217.16	0.006749	167.00	1.00E-07
34	0.074014	217.91	0.007542	167.00	1.00E-07
35	0.078477	218.65	0.008418	167.00	1.00E-07
36	0.083159	219.38	0.009386	167.00	1.00E-07
37	0.088069	220.09	0.010453	167.00	1.00E-07
38	0.093215	220.80	0.011628	167.00	1.00E-07
39	0.098601	221.49	0.012922	167.00	1.00E-07
40	0.104238	222.18	0.014343	167.00	1.00E-07
41	0.110131	222.86	0.015903	167.00	1.00E-07
42	0.116288	223.52	0.017613	167.00	1.00E-07
43	0.122717	224.18	0.019485	167.00	1.00E-07
44	0.129425	224.83	0.021531	167.00	1.00E-07
45	0.136419	225.48	0.023768	167.00	1.00E-07
46	0.143705	226.11	0.026206	167.00	1.00E-07
47	0.151287	226.74	0.028864	167.00	1.00E-07
48	0.159183	227.35	0.031754	167.00	1.00E-07
49	0.167389	227.96	0.034897	167.00	1.00E-07
50	0.175905	228.57	0.038306	167.00	1.00E-07
51	0.184762	229.16	0.042002	167.00	1.00E-07
52	0.193944	229.75	0.046004	167.00	1.00E-07
53	0.203451	230.33	0.050332	167.00	1.00E-07
54	0.213298	230.91	0.055004	167.00	1.00E-07
55	0.223500	231.47	0.060045	167.00	1.00E-07
56	0.234043	232.03	0.065473	167.00	1.00E-07
57	0.244954	232.58	0.071314	167.00	1.00E-07
58	0.256206	233.13	0.077588	167.00	1.00E-07
59	0.267813	233.67	0.084322	167.00	1.00E-07
60	0.279789	234.20	0.091539	167.00	1.00E-07
61	0.292135	234.72	0.099261	167.00	1.00E-07
62	0.304822	235.24	0.107517	167.00	1.00E-07
63	0.317892	235.75	0.116327	167.00	1.00E-07
64	0.331318	236.26	0.125723	167.00	1.00E-07
65	0.345113	236.76	0.135724	167.00	1.00E-07
66	0.359262	237.25	0.146358	167.00	1.00E-07
67	0.373767	237.73	0.157650	167.27	1.00E-07
68	0.388642	238.21	0.169626	167.92	1.00E-07
69	0.403856	238.68	0.182309	168.58	1.00E-07
70	0.419411	239.14	0.195720	169.22	1.00E-07
71	0.435320	239.60	0.209881	169.87	1.23E-07
72	0.451570	240.05	0.224818	173.02	2.17E-07

Table A1. (continued)

Level Number	6 mb Sigma	6 mb Temperature	500 mb Sigma	500 mb Temperature	Water Vapor
73	0.468144	240.49	0.240554	176.16	3.73E-07
74	0.485030	240.93	0.257109	179.30	6.28E-07
75	0.502225	241.36	0.274503	182.42	1.03E-06
76	0.519732	241.79	0.292735	185.52	1.67E-06
77	0.537533	242.20	0.311826	188.61	2.64E-06
78	0.555616	242.61	0.331816	191.69	4.10E-06
79	0.573951	243.02	0.352664	194.74	6.25E-06
80	0.592551	243.41	0.374431	197.76	9.37E-06
81	0.611403	243.80	0.397096	200.77	1.38E-05
82	0.630461	244.18	0.420661	203.74	2.01E-05
83	0.649742	244.56	0.445123	206.69	2.87E-05
84	0.669200	244.93	0.470485	209.60	4.04E-05
85	0.688850	245.29	0.496745	212.48	5.60E-05
86	0.708648	245.65	0.523884	215.32	7.66E-05
87	0.728579	245.99	0.551881	218.12	0.000103
88	0.748643	246.33	0.580757	220.87	0.000137
89	0.768796	246.67	0.610432	223.57	0.000181
90	0.789023	247.00	0.640926	226.22	0.000234
91	0.809294	247.32	0.672198	228.82	0.000300
92	0.829595	247.63	0.704210	231.35	0.000379
93	0.849911	247.93	0.736920	233.82	0.000473
94	0.870211	248.23	0.770309	236.23	0.000584
95	0.890468	248.52	0.804297	238.56	0.000713
96	0.910650	248.81	0.838865	240.81	0.000860
97	0.930729	249.09	0.873932	242.99	0.001025
98	0.950705	249.36	0.909478	245.09	0.001210
99	0.970532	249.62	0.945403	247.11	0.0014146
100	0.990182	249.87	0.981648	249.05	0.0015243
101	1.000000	*250.00*	1.000000	*250.00*	

[a]Sigma values are terrain-following coordinates that reflect the ratio of the local pressure level to the surface pressure ($\sigma = 1.0$ at the surface). Temperature value n reflects the temperature of layer n, which sits between levels n and $n + 1$. Temperatures at level 101 (italicized) are surface temperatures, and coincide with level 101. Water vapor mixing ratio value n likewise reflects value of layer n.

References

Ambartzumian, V. (1936), The effect of the absorption lines on the radiative equilibrium of the outer layers of the stars, *Publ. Obs. Astron. Univ. Leningrad*, *6*, 7–18.

Baranov, Y. I., W. J. Lafferty, and G. T. Fraser (2004), Infrared spectrum of the continuum and dimer absorption in the vicinity of the O_2 vibrational fundamental in O_2/CO_2 mixtures. *J. Mol. Spectrosc.*, *228*, 432–440, doi:10.1016/j.jms.2004.04.010.

Briegleb, B. P. (1992), Delta-Eddington approximation for solar radiation in the NCAR community climate model, *J. Geophys. Res.*, *97*, 7603–7612, doi:10.1029/92JD00291.

Carr, M. H. (1996), *Water on Mars*, 248 pp., Oxford Univ. Press, Oxford, U. K.

Chou, M.-D. (1992), A solar radiation model for use in climate studies, *J. Atmos. Sci.*, *49*, 762–772, doi:10.1175/1520-0469(1992)049<0762:ASRMFU>2.0.CO;2.

Chou, M.-D., and K.-T. Lee (1996), Parameterizations for the absorption of solar radiation by water vapor and ozone, *J. Atmos. Sci.*, *53*, 1203–1208, doi:10.1175/1520-0469(1996)053<1203:PFTAOS>2.0.CO;2.

Christensen, P. R., et al. (2001), Mars Global Surveyor Thermal Emission Spectrometer experiment: Investigation description and surface science results, *J. Geophys. Res.*, *106*, 23,823–23,871, doi:10.1029/2000JE001370.

Clough, S. A., M. J. Iacono, and J.-L. Moncet (1992), Line-by-line calculation of atmospheric fluxes and cooling rates: Application to water vapor, *J. Geophys. Res.*, *97*, 15,761–15,785, doi:10.1029/92JD01419.

Clough, S. A., M. W. Shephard, E. J. Mlawer, J. S. Delamere, M. J. Iacono, K. Cady-Pereira, S. Boukabara, and P. D. Brown (2005), Atmospheric radiative transfer modeling: A summary of the AER codes, short communication, *J. Quant. Spectrosc. Radiat. Transf.*, *91*, 233–244, doi:10.1016/j.jqsrt.2004.05.058.

Crisp, D., S. B. Fels, and M. D. Schwarzkopf (1986), Approximate methods for finding CO_2 15-μm transmission in planetary atmospheres, *J. Geophys. Res.*, *91*, 11,851–11,866, doi:10.1029/JD091iD11p11851.

Edwards, J. M., and A. Slingo (1996), Studies with a flexible new radiation code. I: Choosing a configuration for a large-scale model, *Q. J. R. Meteorol. Soc.*, *122*, 689–719, doi:10.1002/qj.49712253107.

Eymet, V., R. Fournier, J.-L. Dufresne, S. Lebonnois, F. Hourdin, and M. A. Bullock (2009), Net exchange parameterization of thermal infrared radiative transfer in Venus' atmosphere, *J. Geophys. Res.*, *114*, E11008, doi:10.1029/2008JE003276.

Fischer, J., R. R. Gamache, A. Goldman, L. S. Rothman, and A. Perrin (2003), Total internal partition sums for molecular species in the 2000 edition of the HITRAN database, *J. Quant. Spectrosc. Radiat. Transfer*, *82*, 401–412, doi:10.1016/S0022-4073(03)00166-3.

Forget, F., F. Hourdin, R. Rournier, C. Hourdin, O. Talagrand, M. Collins, S. R. Lewis, P. L. Read, and J.-P. Huot (1999), Improved general circulation models of the Martian atmosphere from the surface to above 80 km, *J. Geophys. Res.*, *104*, 24,155–24,175, doi:10.1029/1999JE001025.

Fu, Q., and K. N. Liou (1992), On the correlated k-distribution method for radiative transfer in nonhomogeneous atmospheres, *J. Atmos. Sci.*, *49*, 2139–2156, doi:10.1175/1520-0469(1992)049<2139:OTCDMF>2.0.CO;2.

González-Galindo, F., M. A. López-Valverde, M. Angelats, I. Coll, and F. Forget (2005), Extension of a Martian general circulation model to thermospheric altitudes: UV heating and photochemical models, *J. Geophys. Res.*, *110*, E09008, doi:10.1029/2004JE002312.

Goody, R. M., and Y. L. Yung (1995), *Atmospheric Radiation: Theoretical Basis*, 544 pp., Oxford Univ. Press, Oxford, U. K.

Gough, D. O. (1981), Solar interior structure and luminosity variations, *Sol. Phys.*, *74*, 21–34, doi:10.1007/BF00151270.

Gruszka, M., and A. Borysow (1997), Roto-translational collision-induced absorption of CO_2 for the atmosphere of Venus at frequencies from 0 to 250 cm^{-1}, at temperatures from 200 to 800 K, *Icarus*, *129*, 172–177, doi:10.1006/icar.1997.5773.

Halevy, I., R. T. Pierrehumbert, and D. P. Schrag (2009), Radiative transfer in CO_2-rich paleoatmospheres, *J. Geophys. Res.*, *114*, D18112, doi:10.1029/2009JD011915.

Haqq-Misra, J. D., S. D. Domagal-Goldman, P. J. Kasting, and J. F. Kasting (2008), A revised hazy methane greenhouse for the Archean Earth, *Astrobiology*, *8*, 1127–1137, doi:10.1089/ast.2007.0197.

Hourdin, F. (1992), A new representation of the absorption by the CO_2 15-μm band for a Martian general circulation model, *J. Geophys. Res.*, *97*, 18,319–18,335, doi:10.1029/92JE01985.

Humlíček, J. (1979), An efficient method for evaluation of the complex probability function: The Voigt function and its derivatives, *J. Quant. Spectrosc. Radiat. Transfer*, *21*, 309–313, doi:10.1016/0022-4073(79)90062-1.

Humlíček, J. (1982), Optimized computation of the Voigt and complex probability functions, *J. Quant. Spectrosc. Radiat. Transfer*, *27*, 437–444, doi:10.1016/0022-4073(82)90078-4.

Johnson, S. S., M. A. Mischna, T. L. Grove, and M. T. Zuber (2008), Sulfur-induced greenhouse warming on early Mars, *J. Geophys. Res.*, *113*, E08005, doi:10.1029/2007JE002962.

Kasting, J. F. (1991), CO_2 condensation and the climate of early Mars, *Icarus*, *94*, 1–13, doi:10.1016/0019-1035(91)90137-I.

Kasting, J. F., J. B. Pollack, and D. Crisp (1984), Effects of high CO_2 levels on surface temperature and atmospheric oxidation state of the early Earth, *J. Atmos. Chem.*, *1*, 403–428, doi:10.1007/BF00053803.

Kato, S., T. P. Ackerman, J. H. Mather, and E. E. Clothiaux (1999), The *k*-distribution method and correlated-*k* approximation for a shortwave radiative transfer model, *J. Quant. Spectrosc. Radiat. Transfer*, *62*, 109–121, doi:10.1016/S0022-4073(98)00075-2.

Kylling, A., K. Stamnes, and S.-C. Tsay (1995), A reliable and efficient two-stream algorithm for spherical radiative transfer: Documentation of accuracy in realistic layered media, *J. Atmos. Chem.*, *21*, 115–150, doi:10.1007/BF00696577.

Lacis, A. A., and V. Oinas (1991), A description of the correlated k distribution method for modeling nongray gaseous absorption, thermal emission and multiple scattering in vertically inhomogeneous atmospheres, *J. Geophys. Res.*, *96*, 9027–9063, doi:10.1029/90JD01945.

Lebedinsky, A. I. (1939), Radiative equilibrium in the Earth's atmosphere, *Proc. Leningrad Univ. Ser. Math.*, *3*(31), 152–175.

Lee, C., W. G. Lawson, M. I. Richardson, J. L. Anderson, N. Collins, T. Hoar, and M. Mischna (2011), Demonstration of ensemble data assimilation for Mars using DART, MarsWRF and radiance observations from MGS TES, *J. Geophys. Res.*, *116*, E11011, doi:10.1029/2011JE003815.

Lian, Y., M. I. Richardson, C. E. Newman, C. Lee, A. D. Toigo, M. A. Mischna, and J.-M. Campin (2012), The Ashima/MIT Mars GCM and argon in the Martian atmosphere, *Icarus*, *218*, 1043–1070, doi:10.1016/j.icarus.2012.02.012.

Liou, K. N. (2002), *An Introduction to Atmospheric Radiation*, 2nd ed., 583 pp., Academic, San Diego, Calif.

Meadows, V. S., and D. Crisp (1996), Ground-based near-infrared observations of the Venus nightside: The thermal structure and water abundance near the surface, *J. Geophys. Res.*, *101*, 4595–4622, doi:10.1029/95JE03567.

Mischna, M. A., J. F. Kasting, A. Pavlov, and R. Freedman (2000), Influence of carbon dioxide clouds on early Martian climate, *Icarus*, *145*, 546–554, doi:10.1006/icar.2000.6380.

Mlawer, E. J., S. J. Taubman, P. D. Brown, M. J. Iacono, and S. A. Clough (1997), Radiative transfer for inhomogeneous atmospheres: RRTM, a validated correlated-k model for the longwave, *J. Geophys. Res.*, *102*, 16,663–16,682, doi:10.1029/97JD00237.

Olivero, J. J., and R. L. Longbothum (1977), Empirical fits to the Voigt line width: A brief review, *J. Quant. Spectrosc. Radiat. Transfer*, *17*, 233–236, doi:10.1016/0022-4073(77)90161-3.

Pavlov, A. A., J. F. Kasting, L. L. Brown, K. A. Rages, and R. Freedman (2000), Greenhouse warming by CH_4 in the atmosphere of early Earth, *J. Geophys. Res.*, *105*, 11,981–11,990, doi:10.1029/1999JE001134.

Perrin, M. Y., and J. M. Hartmann (1989), Temperature-dependent measurements and modeling of absorption by CO_2–N_2 mixtures in the far linewings of the 4.3 μm CO_2 band, *J. Quant. Spectrosc. Radiat. Transfer*, *42*, 311–317, doi:10.1016/0022-4073(89)90077-0.

Pollack, J. B., C. B. Leovy, P. W. Greiman, and Y. Mintz (1981), A Martian general circulation experiment with large topography, *J. Atmos. Sci.*, *38*, 3–29, doi:10.1175/1520-0469(1981)038<0003:AMGCEW>2.0.CO;2.

Pollack, J. B., R. M. Haberle, J. Schaeffer, and H. Lee (1990), Simulations of the general circulation of the Martian atmosphere: I. Polar processes, *J. Geophys. Res.*, *95*, 1447–1473, doi:10.1029/JB095iB02p01447.

Press, W. H., S. A. Teukolsky, W. T. Vetterling, and B. P. Flannery (1996), *Numerical Recipes in Fortran 90*, 576 pp., Cambridge Univ. Press, Cambridge, U. K.

Putzig, N. E., M. T. Mellon, K. A. Kretke, and R. E. Arvidson (2005), Global thermal inertia and surface properties of Mars from the MGS mapping mission, *Icarus*, *173*, 325–341, doi:10.1016/j.icarus.2004.08.017.

Richardson, M. I., A. D. Toigo, and C. E. Newman (2007), PlanetWRF: A general purpose, local to global numerical model for planetary atmospheric and climate dynamics, *J. Geophys. Res.*, *112*, E09001, doi:10.1029/2006JE002825.

Rothman, L. S., et al. (1998), The HITRAN molecular spectroscopic database and HAWKS (HITRAN Atmospheric Workstation): 1996 edition, *J. Quant. Spectrosc. Radiat. Transfer*, *60*, 665–710, doi:10.1016/S0022-4073(98)00078-8.

Rothman, L. S., et al. (2009), The HITRAN 2008 molecular spectroscopic database, *J. Quant. Spectrosc. Radiat. Transfer*, *110*, 533–572, doi:10.1016/j.jqsrt.2009.02.013.

Sackmann, I. J., and A. I. Boothroyd (2003), Our Sun. V. A bright young Sun consistent with helioseismology and warm temperatures on ancient Earth and Mars, *Astrophys. J.*, *583*, 1024–1039, doi:10.1086/345408.

Segura, A., V. S. Meadows, J. F. Kasting, D. Crisp, and M. Cohen (2007), Abiotic formation of O_2 and O_3 in high-CO_2 terrestrial atmospheres, *Astron. Astrophys.*, *472*(2), 665–679, doi:10.1051/0004-6361:20066663.

Segura, T. L., O. B. Toon, and A. Colaprete (2008), Modeling the environmental effects of moderate-sized impacts on Mars, *J. Geophys. Res.*, *113*, E11007, doi:10.1029/2008JE003147.

Solomon, S. C., et al. (2005), New perspectives on ancient Mars, *Science*, *307*, 1214–1220, doi:10.1126/science.1101812.

Toon, O. B., C. P. McKay, T. P. Ackerman, and K. Santhanam (1989), Rapid calculation of radiative heating rates and photodissociation rates in inhomogeneous multiple scattering atmospheres, *J. Geophys. Res.*, *94*, 16,287–16,301, doi:10.1029/JD094iD13p16287.

Van Vleck, J. H., and D. L. Huber (1977), Absorption, emission, and linebreadths: Semi-historical perspective, *Rev. Mod. Phys.*, *49*(4), 939–959, doi:10.1103/RevModPhys.49.939.

Van Vleck, J. H., and V. F. Weisskopf (1945), On the shape of collision-broadened lines, *Rev. Mod. Phys.*, *17*(2–3), 227–236, doi:10.1103/RevModPhys.17.227.

von Paris, P., H. Rauer, J. L. Grenfell, B. Patzer, P. Hedelt, B. Stracke, T. Trautmann, and F. Schreier (2008), Warming the early Earth—CO_2 reconsidered, *Planet. Space Sci.*, *56*, 1244–1259, doi:10.1016/j.pss.2008.04.008.

Wells, R. J. (1999), Rapid approximation to the Voigt/Faddeeva function and its derivatives, *J. Quant. Spectrosc. Radiat. Transfer*, *62*, 29–48, doi:10.1016/S0022-4073(97)00231-8.

Wordsworth, R., F. Forget, and V. Eymet (2010), Infrared collision-induced and far-line absorption in dense CO_2 atmospheres, *Icarus*, *210*, 992–997, doi:10.1016/j.icarus.2010.06.010.